iScience

CellPress
OPEN ACCESS

Article

Myeloid leukemia vulnerabilities embedded in long noncoding RNA locus *MYNRL15*

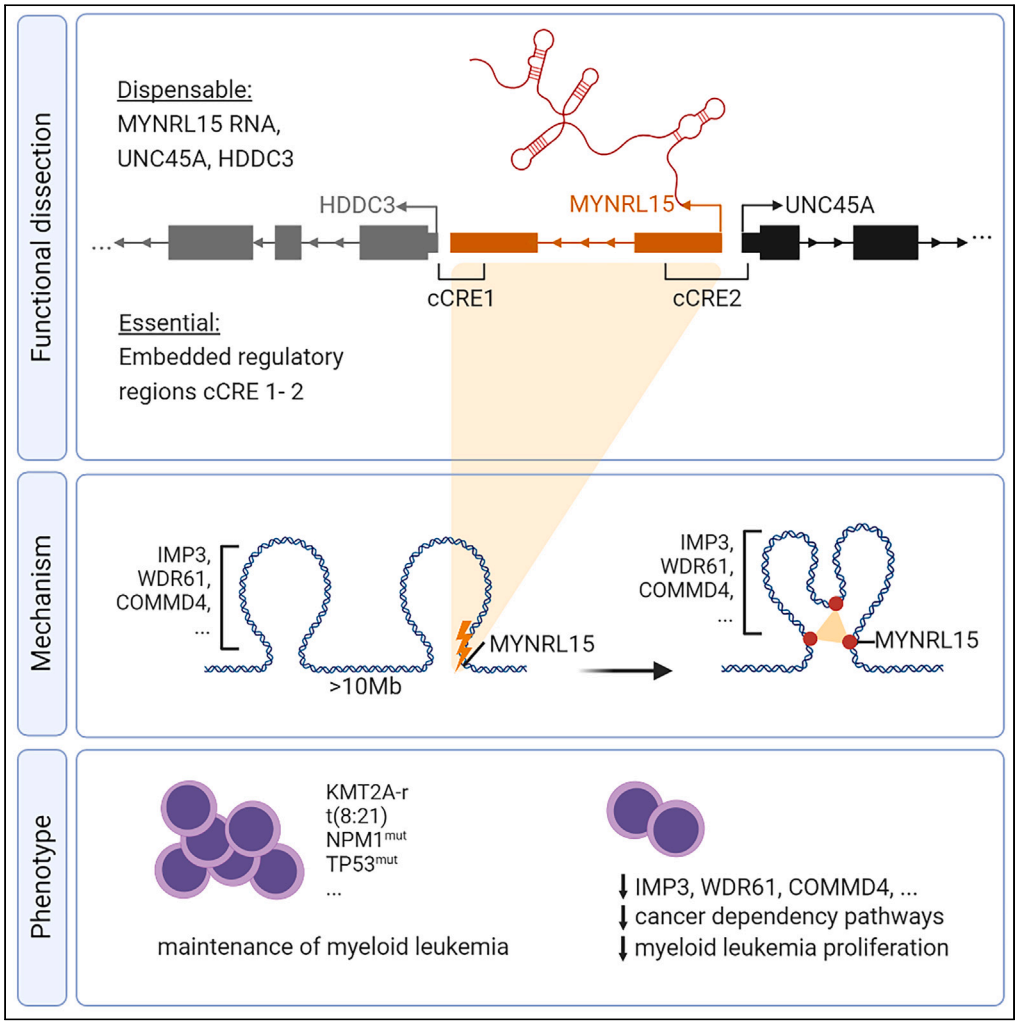

Michelle Ng, Lonneke Verboon, Hasan Issa, ..., Marie-Laure Yaspo, Dirk Heckl, Jan-Henning Klusmann

d.heckl@kinderkrebsstiftung-frankfurt.de (D.H.)
jan-henning.klusmann@kgu.de (J.-H.K.)

Highlights

Long noncoding RNA locus *MYNRL15* identified as a myeloid leukemia dependency

MYNRL15 function is RNA-independent, mediated by two regulatory elements in locus

Perturbation causes long-range looping, downregulation of cancer dependency genes

Perturbation is anti-leukemic in primary AML cells from different genetic backgrounds

Ng et al., iScience *26*, 107844
October 20, 2023
https://doi.org/10.1016/j.isci.2023.107844

iScience

CellPress
OPEN ACCESS

Article

Myeloid leukemia vulnerabilities embedded in long noncoding RNA locus *MYNRL15*

Michelle Ng,[1] Lonneke Verboon,[2,3,4] Hasan Issa,[2,3,4] Raj Bhayadia,[2,3,4] Marit Willemijn Vermunt,[2,4] Robert Winkler,[2,3,4] Leah Schüler,[2,3,4] Oriol Alejo,[1] Konstantin Schuschel,[2,3,4] Eniko Regenyi,[1,5] Dorit Borchert,[6] Michael Heuser,[7] Dirk Reinhardt,[8] Marie-Laure Yaspo,[5] Dirk Heckl,[9,10,*] and Jan-Henning Klusmann[2,3,4,10,11,*]

SUMMARY

The noncoding genome presents a largely untapped source of new biological insights, including thousands of long noncoding RNA (lncRNA) loci. While lncRNA dysregulation has been reported in myeloid malignancies, their functional relevance remains to be systematically interrogated. We performed CRISPRi screens of lncRNA signatures from normal and malignant hematopoietic cells and identified *MYNRL15* as a myeloid leukemia dependency. Functional dissection suggests an RNA-independent mechanism mediated by two regulatory elements embedded in the locus. Genetic perturbation of these elements triggered a long-range chromatin interaction and downregulation of leukemia dependency genes near the gained interaction sites, as well as overall suppression of cancer dependency pathways. Thus, this study describes a new noncoding myeloid leukemia vulnerability and mechanistic concept for myeloid leukemia. Importantly, *MYNRL15* perturbation caused strong and selective impairment of leukemia cells of various genetic backgrounds over normal hematopoietic stem and progenitor cells *in vitro*, and depletion of patient-derived xenografts *in vivo*.

INTRODUCTION

Noncoding sequences comprise 98% of the human genome and harbor a multitude of functional units, including regulatory elements and diverse species of small and long noncoding RNA (lncRNA) loci.[1] Emerging evidence has implicated growing numbers of these noncoding units as players in a variety of physiological and disease processes, including cancer.[2,3] This represents a major opportunity for biologic and therapeutic discovery, especially for malignancies like acute myeloid leukemia (AML), whose treatment has only recently begun to evolve beyond the cytostatic regimen developed in the 1970s.[4] Studies in AML patient cohorts have uncovered lncRNA expression signatures specific to genetic subgroups of AML[5–7] as well as unifying stem cell signatures.[6,8] However, due to their extensive mechanistic diversity,[9] the study of lncRNAs can be more complicated than of other noncoding RNA species, and only a handful of lncRNA loci have undergone extensive functional characterization in AML.[10–13] Thus, despite rapid growth in the field, our knowledge of lncRNA loci and their roles in this disease remains severely limited.

Loosely defined as noncoding transcripts longer than 200 nucleotides, a significant barrier in the characterization of lncRNAs has been the difficulty of unraveling their mechanisms of action. LncRNA loci can occur sense- or antisense-overlapping, head-to-head, or intergenic in relation to protein-coding genes, and besides RNA-mediated *cis* and *trans* action, they can exert *cis*-regulatory effects independent of the transcript itself, through the act of transcription at the locus or through DNA regulatory elements embedded in the locus.[9] In addition, transcriptional regulatory units such as enhancers and promoters can initiate bidirectional transcription, and considerable overlap exists between lncRNA loci and regulatory regions.[14] These mechanisms are also not mutually exclusive, and some lncRNA loci may act through multiple routes. One prominent example is *PVT1*, a lncRNA in the *MYC* locus, which acts as a *bona fide* oncogenic RNA while its promoter functions as a tumor suppressor boundary element.[15] Thus, in-depth functional dissection is required to fully understand the functions of uncharacterized lncRNAs.

[1]Department of Pediatric Hematology and Oncology, Martin Luther University Halle-Wittenberg, 06120 Halle (Saale), Germany
[2]Department of Pediatrics, Goethe University Frankfurt, 60323 Frankfurt (Main), Germany
[3]Frankfurt Cancer Institute, Goethe University Frankfurt, 60323 Frankfurt (Main), Germany
[4]German Cancer Consortium (DKTK), Partner Site Frankfurt/Mainz and German Cancer Research Center (DKFZ), Heidelberg, Germany
[5]Department of Vertebrate Genomics, Max Planck Institute for Molecular Genetics, 14195 Berlin, Germany
[6]Department of Pediatric Hematology and Oncology, Hannover Medical School, 30625 Hannover, Germany
[7]Department of Hematology, Hemostasis, Oncology and Stem Cell Transplantation, Hannover Medical School, 30625 Hannover, Germany
[8]Clinic for Pediatrics III, University Hospital Essen, 45147 Essen, Germany
[9]Institute for Experimental Pediatric Hematology and Oncology, Goethe University Frankfurt, 60323 Frankfurt (Main), Germany
[10]These authors contributed equally
[11]Lead contact
*Correspondence: d.heckl@kinderkrebsstiftung-frankfurt.de (D.H.), jan-henning.klusmann@kgu.de (J.-H.K.)
https://doi.org/10.1016/j.isci.2023.107844

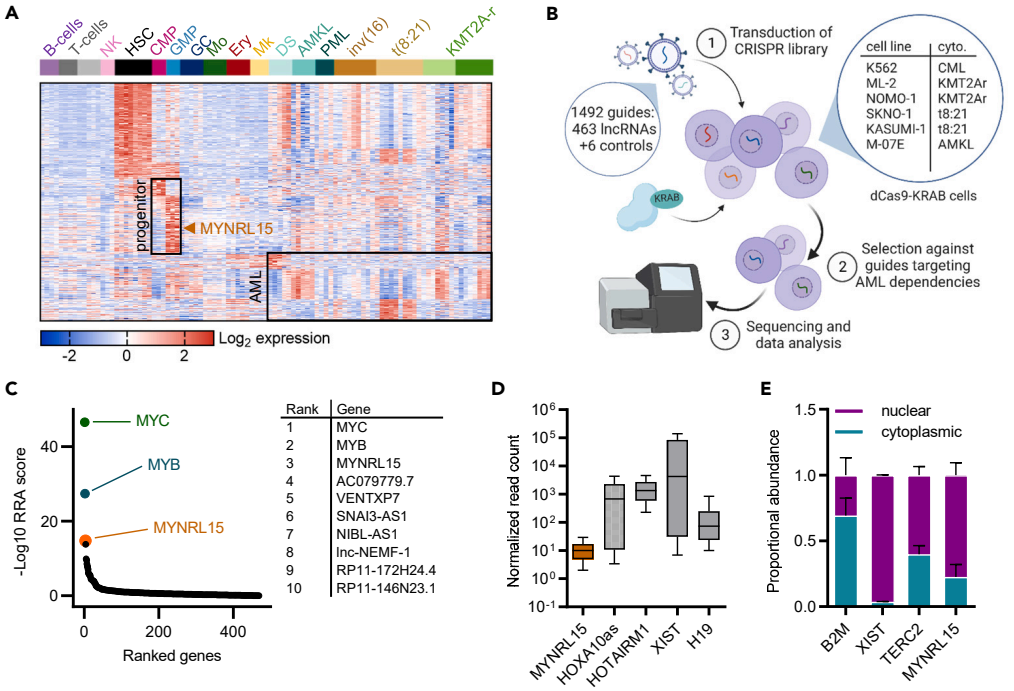

Figure 1. CRISPRi screen of HSPC/AML lncRNA signatures

See also Figures S1 and S2, Table S1.

(A) Expression of HSPC/AML lncRNAs across 12 normal blood cell populations and 46 pediatric AML samples.[6] Signatures of particular interest are outlined. Natural killer cell (NK), hematopoietic stem cell (HSC), common myeloid progenitor (CMP), granulocyte-monocyte progenitor (GMP), granulocyte (GC), monocyte (Mo), erythroid precursor (Ery), megakaryocyte (Mk), Down syndrome-associated myeloid leukemia (DS), non-DS megakaryoblastic leukemia (AMKL), promyelocytic leukemia (PML), *KMT2A*-rearranged leukemia (*KMT2A*-r).

(B) Conceptual workflow for screening HSPC/AML lncRNAs.

(C) Gene essentiality scores from pan-cell line MAGeCK analysis of the CRISPRi screen (6 cell lines, n = 2 biological replicates each). The top hit *MYNRL15* is highlighted behind *MYC* and *MYB*, the positive controls. The top 10 hits are indicated on the right.

(D) Expression of *MYNRL15* compared to *bona fide* lncRNAs in the NCI-TARGET pediatric AML cohort (n = 258). Midline, median; box limits, lower and upper quartiles; whiskers, 10% and 90% quantiles.

(E) Subcellular localization of *MYNRL15* compared to controls *XIST* (nuclear), *TERC* (nuclear), and *B2M* (cytoplasmic), as determined via fractionated qRT-PCR (n = 2 biological replicates, mean ± SEM).

In this study, we set out to identify lncRNAs involved in myeloid leukemia pathogenesis via a CRISPR interference (CRISPRi) screen of expression signatures derived from normal hematopoietic cells and pediatric AML patient samples. Detailed characterization of the top candidate from the screen, *MYNRL15*, suggested an RNA-independent mechanism via two candidate regulatory regions embedded in the locus. Genetic perturbation of these elements was associated with long-range chromatin conformation changes and downregulation of cancer dependency pathways. Importantly, *MYNRL15* perturbation selectively impaired AML cells of multiple genetic backgrounds compared to normal hematopoietic stem and progenitor cells (HSPCs) *in vitro*, and depleted AML xenografts *in vivo*. Thus, we report a new noncoding vulnerability and mechanistic concept for myeloid leukemia.

RESULTS

Systematic interrogation of HSPC/AML lncRNAs via CRISPRi screens

We previously developed a noncoding RNA expression atlas of the human blood system encompassing hematopoietic stem cells (HSCs) and their differentiated progeny, as well as pediatric AML samples.[6] In addition to stem cell signatures reminiscent of those previously established for protein-coding genes,[16,17] we discovered progenitor- and AML subtype-associated lncRNA profiles that could potentially serve as leukemia-specific targets, given their absence in HSCs (Figure 1A). To probe this resource for functionality and identify myeloid leukemia vulnerabilities, we conducted a CRISPRi-based dropout screen of 463 lncRNA genes from 8 distinct signatures in 6 human leukemia cell lines (Figure 1B). Five cell lines were selected to represent prominent cytogenetic subgroups of AML—ML-2, NOMO-1 (*KMT2A*-rearranged), SKNO-1, KASUMI-1 (standard risk with t[8:21]), and M-07E (high risk with inv[16])—and we also included the well-studied erythroleukemia line K562. Stable dCas9-KRAB expressing cell lines were transduced with a single guide RNA (sgRNA) library targeted to lncRNA transcription start sites (TSSs) (Table S1; see STAR methods for design principles), and sgRNA abundances were quantified via next generation sequencing before

and after 18 population doublings. Model-based analysis of genome-wide CRISPR-Cas9 knockout (MAGeCK)[18] was used to call essential lncRNAs required for leukemia cell proliferation. While most lncRNA dependencies were identified in only one cell line, consistent with previously reported lncRNA screens,[19,20] several were called in two or more cell lines, including *SNAI3-AS1*, *NIPBL-AS1*, *VENTXP7*, *AC079779.5*, and *AC068831.3* (Figures 1C and S1A; Table S1).

Identification of MYNRL15 as a myeloid leukemia dependency locus

Because it emerged as the top candidate overall from our screen, we subsequently focused on *AC068831.3* (ID: ENSG00000224441 in Ensembl v85 [release 07/2016]) (Figures 1C, S1A, and S1B)—hereafter referred to as *MYNRL15* (myeloid leukemia noncoding regulatory locus on chromosome 15). We validated the anti-leukemic effect of *MYNRL15* knockdown in individual proliferation assays, using three effective sgRNAs in all 6 cell lines (Figures S1C and S1D; note, one library sgRNA did not achieve efficient knockdown and was replaced). *MYNRL15* is a low-abundance, nuclear-enriched transcript (Figures 1D and 1E) from the GMP/AML signature (Figures 1A and S2A–S2C). It is transcribed from chromosome 15, where it is flanked by two protein-coding genes: *UNC45A* and *HDDC3* (Figure 2A). Given the effect of the CRISPRi system on the expression of these neighboring genes (Figures 2B and S1C right), a range of gain- and loss-of-function approaches were necessary to delineate the source of the *MYNRL15* knockdown phenotype (Figures 2 and S2). Whereas CRISPR mediated excision of *MYNRL15* using dual sgRNA vectors recapitulated the effect produced by CRISPRi, targeting the transcript via shRNAs and LNA-gapmeRs had little impact on proliferation (Figures 2C, S2A, and S2B), as did CRISPR-mediated promoter excision and splice site disruption (Figures 2C, S2C, and S2E). Both protein-coding neighbors also appeared to be dispensable, as determined by individual and combined CRISPR-Cas9 mediated knockout of UNC45A and HDDC3, as well as CRISPRi-mediated knockdown of *HDDC3* (Figures 2C, S2B, S2C, and S2E). Overexpression of *MYNRL15* cDNAs additionally failed to rescue the CRISPRi knockdown phenotype (Figure 2D). Taken together, these data indicate that neither of the flanking protein-coding genes, nor the *MYNRL15* transcript itself, is responsible for the function of the locus in myeloid leukemia cells. Rather, they suggest that *MYNRL15* acts as an expressed noncoding regulatory locus with RNA-independent function.

Functional dissection of the MYNRL15 locus reveals crucial regulatory regions

Given the apparent dispensability of *UNC45A*, *HDDC3*, and the *MYNRL15* transcript itself in leukemia cells, we hypothesized that *MYNRL15* may harbor DNA regulatory elements which drive its leukemia dependency phenotype. To test this hypothesis, we functionally dissected the *MYNRL15* locus via complementary CRISPRi and CRISPR-Cas9 screens tiling a 15 kb area centered on *MYNRL15*. Cell lines (K562, ML-2, M-07E, and KASUMI-1) stably expressing either dCas9-KRAB or Cas9 were transduced with a sgRNA library covering the region at a mean density of 0.11 sgRNAs per bp (Table S2), with the expectation that key areas would be demarcated by hubs of depleting sgRNAs. Notably, the *MYNRL15* locus contains several regions that exhibit features characteristic of *cis*-regulatory elements, such as H3K4Me1 and H3K27Ac histone marks, DNase hypersensitivity, and transcription factor occupancy including multiple CTCF and cohesin binding sites (Figure 3A). The tiling screens uncovered two regions where accessibility and integrity were required by the leukemia cells, both of which overlapped CpG islands and divergent H3K27Ac/H3K4me1 signals (Figures 3B and S3A). Both regions enhanced reporter gene expression, singly and in combination, when cloned upstream of a minimal promoter in dual luciferase assays (Figure S3B). Together, these data nominate the crucial regions as functional sequences and candidate *cis*-regulatory elements (cCREs C1 and C2). The Cas9 based mutagenesis strategy also reiterated that leukemia cells do not seem particularly dependent on the UNC45A and HDDC3 coding sequences, indicating that local enhancer functions on these genes are unlikely to explain the anti-leukemic effect of *MYNRL15* perturbation.

RNA profiling suggests regulation of cancer dependency pathways by MYNRL15

Aiming to identify the target genes and pathways controlled by the *MYNRL15* locus, we next performed RNA sequencing following the disruption of cCREs C1 and C2 via CRISPR-Cas9 mediated induction of DNA double-strand breaks (hereafter referred to simply as *MYNRL15* perturbation). We opted for the CRISPR-Cas9 system in an effort to achieve a narrower perturbation of *MYNRL15* and mitigate the longer-range suppression caused by CRISPRi; however, expression of the neighboring genes *UNC45A* and *HDDC3* were still affected (Figure S4C). We selected two guides from each cCRE, all of which robustly depleted K562 and ML-2 leukemia cells (Figure 3C). This phenotype was underpinned by global changes in gene expression (Figures 3D–3F and S4A–S4C), including the dramatic suppression of cancer dependency signatures related to proliferation and metabolism across both cell lines and two time points (Figures 3E, 3F, and S4C). 531 genes were commonly deregulated across both K562 and ML-2 cells (167 up, 364 down), including 20 downregulated genes from chromosome 15 (Figure 3D). The downregulated genes were enriched for ontology terms related to the ribosome and RNA splicing (Figure 3E)—an observation that was confirmed by GSEA (Figure 3F), implicating *MYNRL15* in the maintenance of these processes. GSEA further revealed suppression of other cancer-essential pathways such as oxidative phosphorylation and DNA replication, as well as of well-known oncogenic programs such as MYC target genes, upon *MYNRL15* perturbation (Figure 3F). However, while these data support *MYNRL15*'s leukemia dependency phenotype, they represent general pathways and no obvious candidate targets stood out (e.g., outstanding fold change and significance, known cancer genes, near the locus), leading us to consider the possibility that the locus may regulate multiple genes in a genomic neighborhood[21] in a subtler manner. To explore this alternative, we applied a sliding window approach to GSEA by using custom gene sets composed of 1 Mb, 2 Mb, 5 Mb, and 10 Mb sections of chromosome 15 (see STAR methods for details). This revealed positional gene sets that were deregulated following *MYNRL15* perturbation, including the area around *MYNRL15* and a distal region in both K562 and ML-2 (Figures 3G and S4D), and others that were unique to one of the cell lines (Figure S4E).

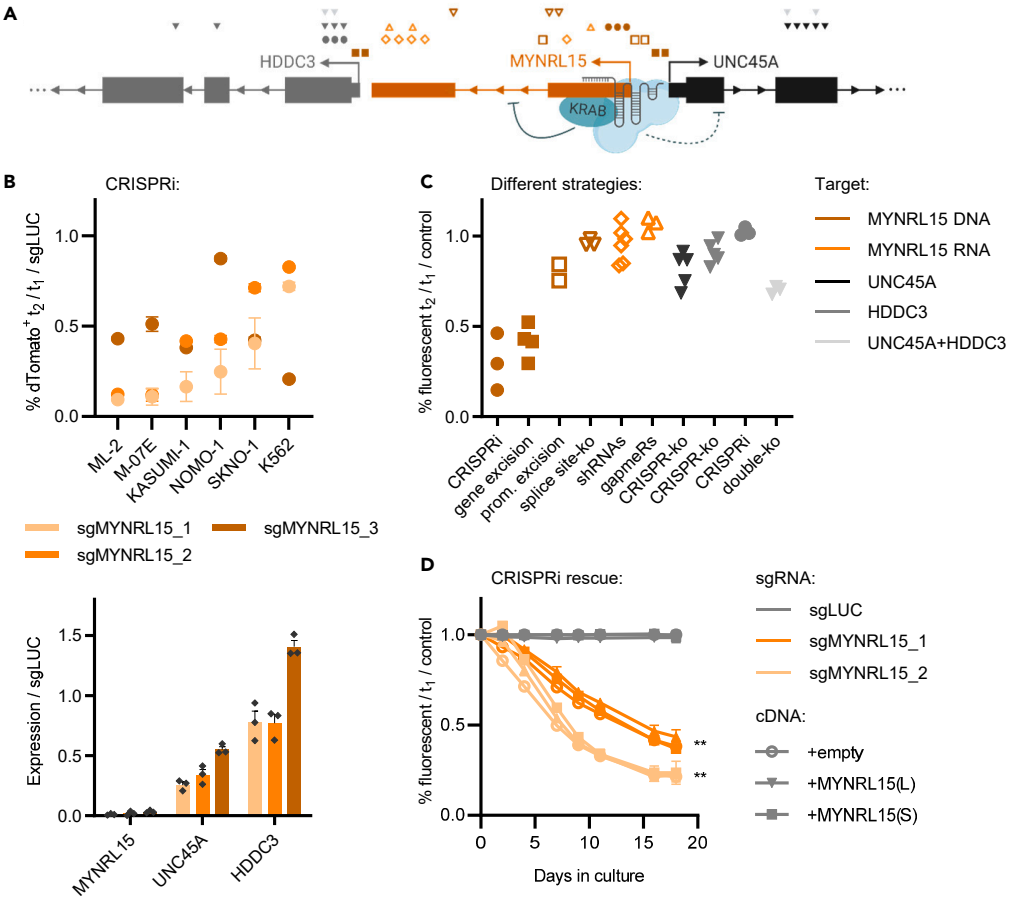

Figure 2. Characterization of *MYNRL15* as a myeloid leukemia dependency locus

See also Figure S3.

(A) Schematic of the *MYNRL15* locus, including the target sites of the different perturbation constructs (not to scale). Target gene: *MYNRL15* (orange), *UNC45A* (black), *HDDC3* (gray), *UNC45A* + *HDDC3* (light gray). Perturbation strategy: CRISPRi (filled circle), gene excision (filled square), promoter excision (empty square), splice site disruption (empty triangle), RNAi (empty diamond), LNA-gapmeRs (empty triangle), CRISPR-Cas9 mediated knockout (filled triangle).

(B) Top: Endpoint depletion values from fluorescence-based proliferation assays that used CRISPRi to knock down *MYNRL15* in different cell lines (same data as in Figure S1D; n = 2 biological replicates, mean ± SEM). The data are normalized to day 0 and to the non-targeting control (sgLUC). Bottom: expression of *MYNRL15* and its flanking coding genes after targeting the CRISPRi system to the *MYNRL15* TSS, as determined via qRT-PCR (n = 3 biological replicates, mean ± SEM; data normalized to the non-targeting control).

(C) Endpoint depletion values from fluorescence-based proliferation assays using different perturbation strategies to target *MYNRL15*, *UNC45A*, and/or *HDDC3*. Each point represents one vector used for perturbation (mean of n = 3 biological replicates shown). The data are normalized to day 0 and to the non-targeting control.

(D) Fluorescence-based proliferation assays using *MYNRL15* cDNAs to rescue the CRISPRi depletion phenotype (n = 2 biological replicates, mean ± SEM; double-positive sgRNA+cDNA cells are shown). **p < 0.01 (two-tailed, unpaired t-test); all conditions share the same p value. Colors denote sgRNA vectors, shapes denote cDNA vectors. Long isoform (L), short isoform (S).

(C and D) These experiments were performed in ML-2 cells.

Altered chromosome 15 architecture underlies the MYNRL15 perturbation phenotype

Given the deregulation of chromosome 15 neighborhoods upon *MYNRL15* perturbation, we explored whether this may be associated with changes in chromatin conformation using next generation Capture-C (NG Capture-C).[22] Because of the strong divergent H3K27Ac/H3K4me1 signal, the CTCF binding site overlapping the element, and the potent perturbation phenotype (Figures 3B and 3C), we focused on *MYNRL15* cCRE C1 and used enrichment probes complementary to this region. In unedited K562 and ML-2 cells, Capture-C revealed extensive local interactions between the *MYNRL15* locus and sequences within a 500 kb radius, with almost no interactions occurring outside of a 2 Mb radius (Figures 4A–4C). Interestingly, *MYNRL15* perturbation had little impact on this local interaction profile, and instead caused the gain two long-range interactions 12 Mb and 15 Mb away from the locus (Figures 4B–4D), indicating larger-scale reorganization of chromosome 15 upon *MYNRL15* perturbation that brings the locus into contact with distal sites. Notably, both the local and gained long-range interactions overlap with contact domain boundaries (Figures 4B–4C, S5A, and S5B). Interestingly, in K562 ChIP-seq data from ENCODE, 24 transcription factors

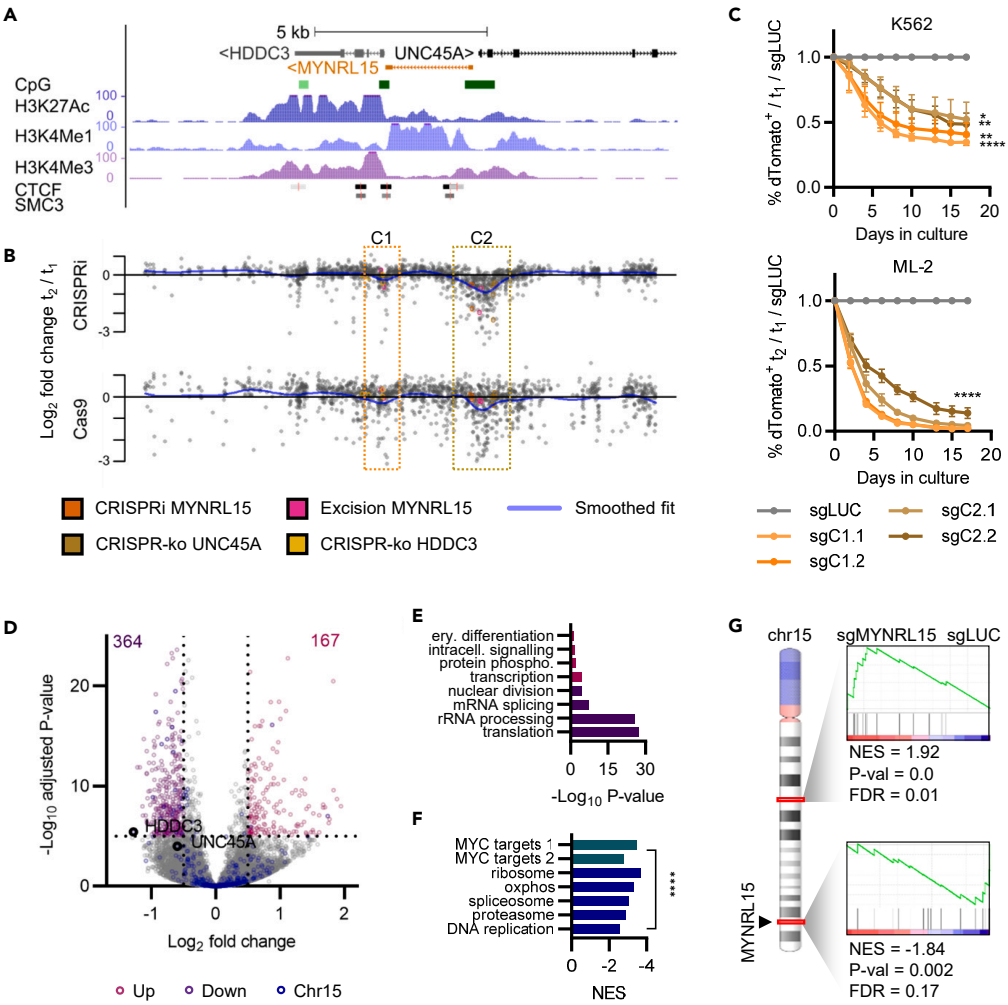

Figure 3. Functional dissection of *MYNRL15* locus reveals crucial regulatory regions

See also Figures S4 and S5, Table S2.

(A) Tracks from the UCSC Genome Browser showing, from top to bottom: gene annotations, CpG islands, histone marks, and CTCF and cohesin occupancy (K562 ChIP-seq data from ENCODE).

(B) Tiling screen results using parallel CRISPRi (top) and CRISPR-Cas9 based (bottom) strategies to interrogate the *MYNRL15* locus shown in a (mean of 4 cell lines, n = 2 biological replicates each). Previously tested sgRNAs are shown in color. A smoothed fit curve is shown in blue. The two cCREs, C1 and C2, are outlined. Positions are to scale to the annotation tracks shown above.

(C) Fluorescence-based proliferation assays using classical CRISPR-Cas9 and individual sgRNAs from C1 and C2 to achieve perturbation of the *MYNRL15* locus (n = 3 biological replicates, mean ± SEM; 2 guides per cCRE, 4 guides in total). The data are normalized to day 0 and to the non-targeting control (sgLUC). *p < 0.05, **p < 0.01, ****p < 0.0001 (two-tailed, unpaired t-tests); where only one set of asterisks is shown, all conditions share the same p value.

(D–G) Differential expression analyses comparing the *MYNRL15* perturbation group (all 4 guides from c; "sgMYNRL15") to the non-targeting control ("sgLUC") in a combined analysis across early (day 3) and late (day 6 and 7, respectively) time points of ML-2 and K562 cells (n = 2 biological replicates per guide).

(D) Volcano plot depicting differential gene expression following *MYNRL15* perturbation, as determined using DESeq2. The most significantly up- and downregulated genes are shown in pink and purple, respectively ($P_{adj} \leq 10^{-5}$, |LFC|≥-0.5); chromosome 15 genes are shown in blue.

(E) Gene ontology terms enriched in the significantly up- (pink) and downregulated (purple) genes from (D), as determined using the DAVID functional annotation tool. Erythroid (ery), intracellular (intracell), phosphorylation (phospho).

(F) Normalized enrichment scores (NES) of cancer dependency gene sets that are downregulated upon *MYNRL15* perturbation. Colors correspond to MSigDB collections H1 "hallmark" (turquoise) and C2 "KEGG pathways" (blue). ****p = 0 (nominal *p* values from GSEA).

(G) Two chromosome 15 positional gene sets (1 Mb windows) that are downregulated upon *MYNRL15* perturbation, including a region around the *MYNRL15* locus (bottom). NES, p values, and FDRs were calculated by GSEA.

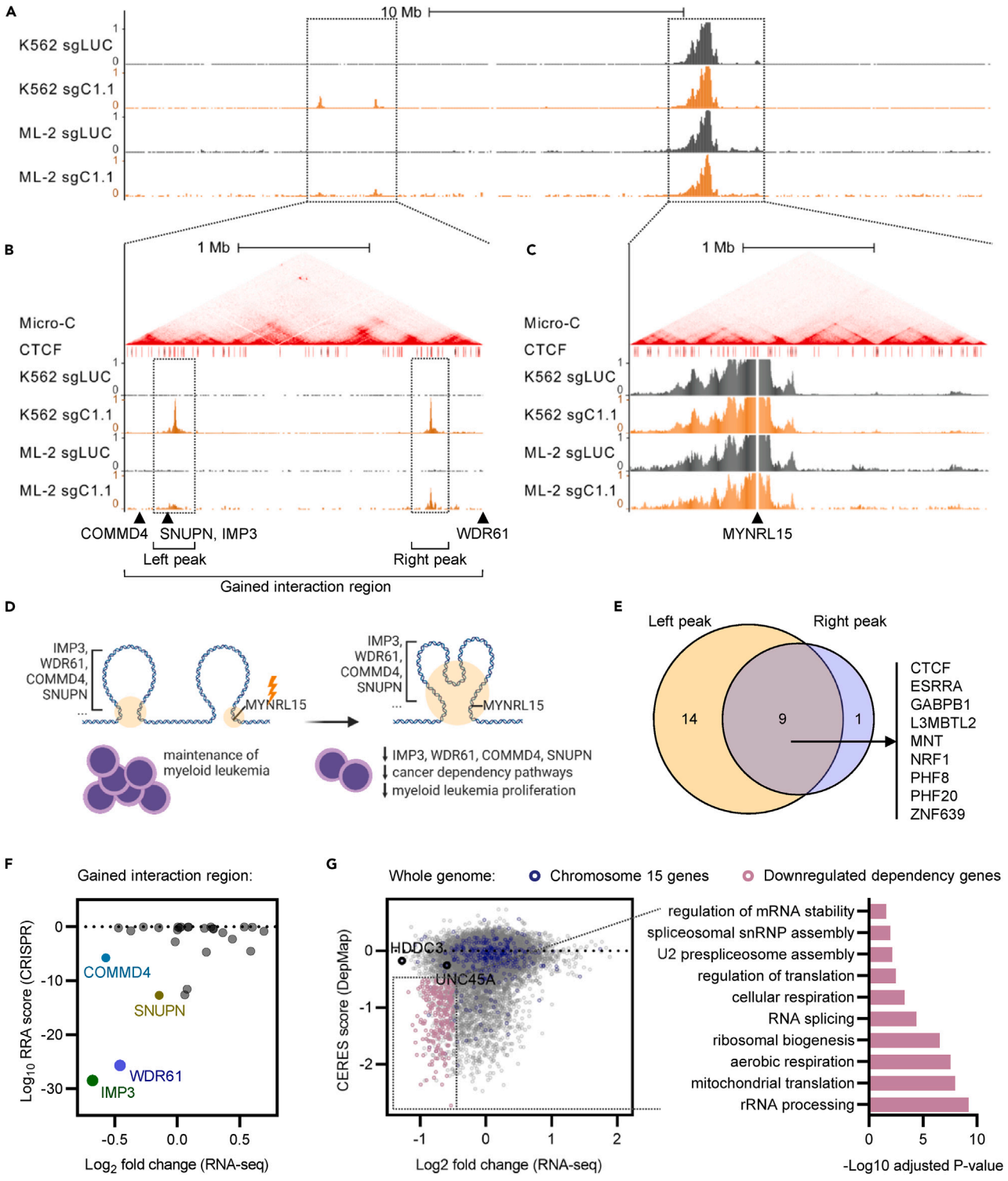

Figure 4. *MYNRL15* perturbation alters chromosome 15 conformation and expression of cancer dependency genes

See also Figure S6, Tables S3 and S4.

(A) NG Capture-C interaction profiles on chromosome 15 in K562 and ML-2 cells, using one guide targeting *MYNRL15* (sgC1.1) and a non-targeting control (sgLUC) (n = 2 biological replicates; viewpoint in C1; smoothing window 2 pixels).

(B and C) Close-ups of the gained distal interaction region and the region around *MYNRL15*, alongside K562 CTCF ChIP-Seq and H1-hESC Micro-C[23] tracks from the UCSC Genome Browser.

Figure 4. *Continued*

(D) Model of chromosome 15 reorganization following *MYNRL15* perturbation.

(E) Venn diagram depicting the 24 transcription factors that bind both C1 and C2, and whether they also bind the gained distal interaction regions (binding sites identified using ENCODE K562 ChIP-seq data).

(F) Integrative analysis of CRISPR-Cas9 screening scores (MAGeCK; n = 2 per cell line) and differential expression after *MYNRL15* perturbation (DESeq2; comparison as in Figures 2D and 2E) for the 29 coding genes located in the gained distal interaction region. A combined analysis of K562 and ML-2 cells is shown.

(G) Left: integrative analysis of genome-wide CRISPR-Cas9 screening scores (DepMap K562 data) and differential expression after *MYNRL15* perturbation (DESeq2; comparison as in Figures 2D and 2E). Downregulated dependency genes are shown in pink ($P_{adj} \leq 10^{-3}$, CERES ≤ -0.5); chromosome 15 genes are shown in blue. Right: gene ontology terms enriched in the downregulated dependency genes, as determined using the DAVID functional annotation tool.

show occupancy in both C1 and C2 (Figure 4E; Table S3). Of these, 9 also bind both gained interaction sites, of which 8 have been described to function in hematopoiesis or leukemia (see Table S3 for PMIDs). We think these would be the most likely candidates for the mediator of the long-range interaction, and this list may serve as a starting point for future studies.

Given the gained long-range chromatin interactions following *MYNRL15* perturbation, we hypothesized that this distal region may be the source of its anti-leukemic phenotype. To probe the region for candidate effectors of the phenotype, we conducted a CRISPR-Cas9 knockout screen of its 29 protein-coding genes (Table S4) and cross-referenced the results with differentially expressed genes identified by RNA sequencing (Figure 3F). Thus, by integrating chromatin conformation, transcriptome, and leukemia dependency information, we found several candidate downstream effector genes of *MYNRL15* perturbation: *IMP3*, *WDR61*, *COMMD4*, and *SNUPN* (Figures 4F and S6C). These genes belong to the gained chromatin interaction region, are downregulated following *MYNRL15* perturbation, and score as leukemia dependencies in the CRISPR-Cas9 knockout screen, suggesting that they contribute to the anti-leukemic phenotype triggered by *MYNRL15* perturbation. In contrast, in the local region around *MYNRL15* (Figure 3G; this gene set is downregulated in GSEA), downregulated and dependency genes are mutually exclusive and are thus unlikely to underlie the anti-leukemic phenotype (Figure S6D; gene essentiality data from DepMap[24]). We note that, genome-wide, over 200 dependency genes belonging to crucial cellular pathways are downregulated after *MYNRL15* perturbation (Figure 4G). The gained chromatin interaction and suppression of *IMP3*, *WDR61*, *COMMD4*, etc. may only be a part of this broad deregulation.

To validate the results of the gained interaction region screen, we performed CRISPR-Cas9 knockout of the top candidates, *IMP3* and *WDR61*, and confirmed that guides targeting these genes depleted K562 and ML-2 cells at a level comparable to *MYNRL15* perturbation (Figure S6E). *IMP3* encodes a component of the 60-80S U3 small nucleolar ribonucleoprotein that is required for early cleavages in pre-18S ribosomal RNA processing.[25] *WDR61* encodes a subunit of the PAF1 complex (PAF1c), which has been reported to stimulate the transcriptional activity of KMT2A and KMT2A-rearranged fusion oncoproteins at *HOX* loci.[26,27] Of note, among the expression changes associated with *MYNRL15* perturbation, signatures related to ribosome biogenesis and function were strongly suppressed (Figures 3E and 3F), and signatures induced by Paf1c inactivation[28]—including the downregulation of Hoxa9 and Meis1 target genes—were also detected (Figure S6F).

In summary, genetic perturbation of *MYNRL15* C1 triggered the formation of a long-range chromatin interaction and the downregulation of several leukemia dependency genes in the distal region. This was associated with the suppression of pro-leukemic PAF1C targets and ribosome-related signatures, among other crucial pathways. These results implicate *MYNRL15* in the maintenance of a permissive chromatin conformation in leukemic cells that assures expression of cancer dependency genes (Figure 4F), although the mediating factor remains unknown.

Anti-leukemic effect of MYNRL15 perturbation in primary cells

MYNRL15 perturbation had anti-leukemic effects across cell lines representative of the wide spectrum of genetic alterations found in AMLs (Figures 1A, 3B, and S1; Table S5), including those important to adult AMLs such as NB-4 (PML:RARA), OCI-AML3 (normal karyotype with NPM1 and DNMT3A mutations), and TF-1 (normal karyotype with TP53) (Figure S7A). To evaluate whether *MYNRL15* dependency is specific to leukemic cells, we leveraged all-in-one lentiviral CRISPR-Cas9 constructs in primary human $CD34^+$ HSPCs from healthy donors and in blasts derived from AML patients (see Table S5 for patient characteristics). The cells were transduced with vectors containing *MYNRL15*-targeting or control sgRNAs, sorted, and seeded in methylcellulose-based media colony-forming assays. Whereas *MYNRL15* perturbation moderately impaired colony formation in $CD34^+$ HSPCs, it had little effect on their replating capacity or differentiation (Figure 5A). In contrast, AML colony-forming units were virtually eradicated across three subgroups of pediatric AML and normal karyotype adult AML samples (8 samples total; Figures 5B–5D), implying that *MYNRL15* perturbation selectively impacts AML cells, and outlining a possible therapeutic window (Figure 5E). Interestingly, we note the presence of interactions between the *MYNRL15* locus and distal upstream regions in $CD34^+$ HSPCs (Figure S7B), suggesting that pre-existing long-range connectivity may contribute to the attenuated effect of *MYNRL15* perturbation in these cells. Altogether, our data suggest that the *MYNRL15* locus is broadly required by myeloid leukemia cells of different subgroups and genetic backgrounds.

To assess the anti-leukemic effect of *MYNRL15* perturbation *in vivo*, we applied CRISPRi-based two-color competitive xenotransplantation assays using AML cell lines and patient-derived xenografts (PDXs) (Figure 5F, see Table S5 for patient characteristics). Importantly, *MYNRL15* perturbation impaired the propagation of two AML cell lines and two PDXs in recipient mice (Figures 5F, S7C, and S7D), confirming its capacity to deplete leukemic cells *in vivo*. Combined with its selective impairment of AML cells, these results provide a proof-of-principle of how *MYNRL15* perturbation may be leveraged as a therapeutic concept.

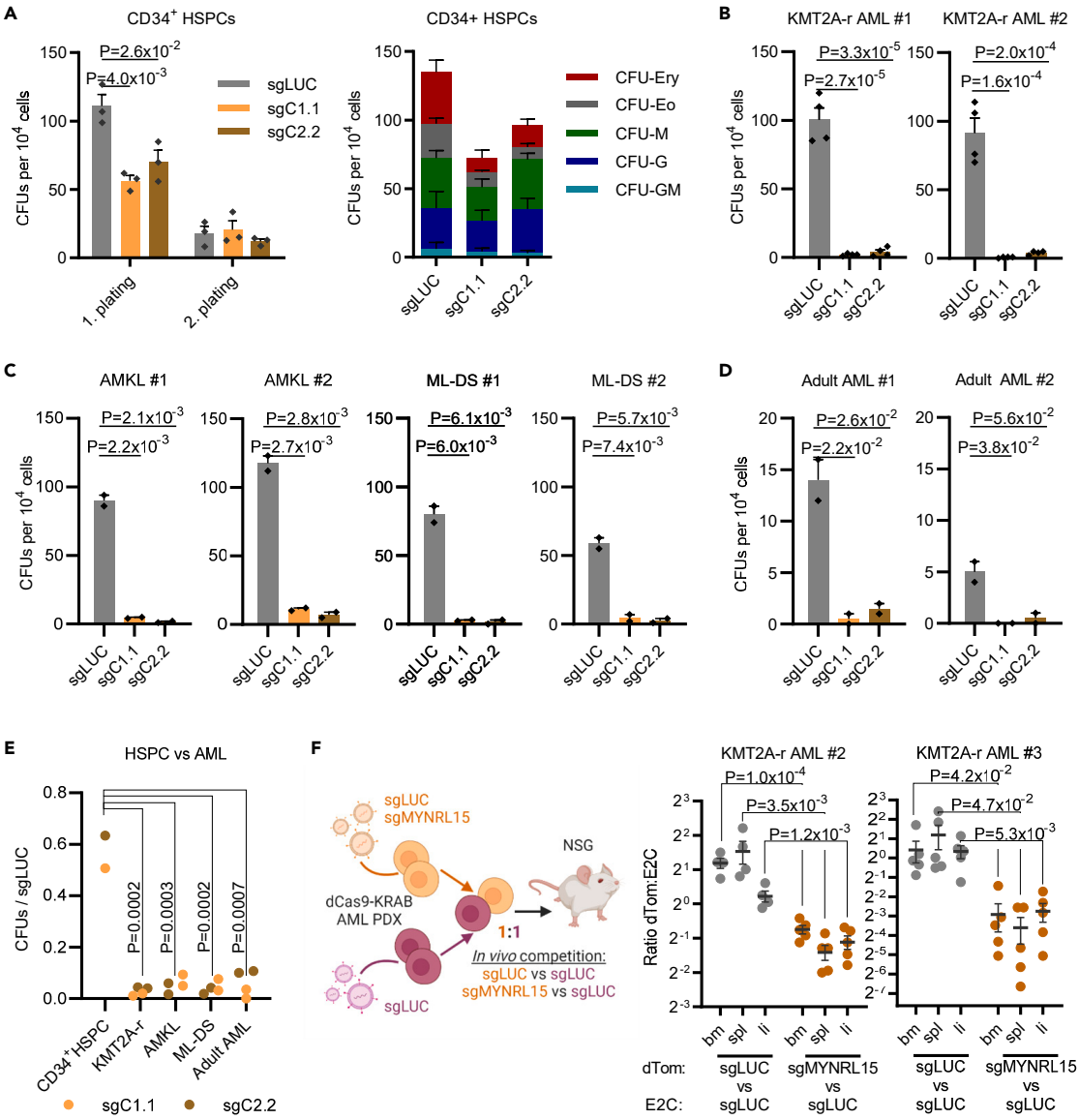

Figure 5. Anti-leukemic effect of *MYNRL15* perturbation in primary cells

See also Figure S7, Table S5.

(A) Colony counts following *MYNRL15* perturbation in CD34$^+$ HSPCs from healthy donors (n = 3 biological replicates; mean ± SEM). Replating capacity (left) and differentiation (right) were evaluated.

(B) Colony counts following *MYNRL15* perturbation in two patient-derived KMT2A-r pediatric AML samples (n = 4 biological replicates; mean ± SEM).

(C) Colony counts following *MYNRL15* perturbation in two AMKL and two ML-DS pediatric AML samples (n = 2 biological replicates; mean ± SEM).

(D) Colony counts following *MYNRL15* perturbation in two normal karyotype adult AML samples (n = 2 biological replicates; mean ± SEM).

(E) Comparison of *MYNRL15* perturbation in CD34$^+$ HSPCs (n = 3 biological replicates) versus 8 AML PDXs belonging to 4 subgroups (2 PDXs per subgroup): *KMT2A*-r (pediatric; n = 4 biological replicates each), AMKL (pediatric; n = 2), ML-DS (pediatric; n = 2) and normal karyotype AML (adult; n = 2). Data are normalized to the non-targeting control. Each dot represents a mean of replicates.

(F) Setup (left) and results (right) of direct two-color *in vivo* competition assays involving CRISPRi mediated perturbation of *MYNRL15* in AML PDXs. The data are presented as ratios of dTomato$^+$ (dTom) to E2Crimson$^+$ (E2C) cells in the bone marrow (bm), spleens (spl), and livers (li) of recipient mice (n = 4 in the AML PDX #2 control group, otherwise n = 5 per group; mean ± SEM).

(A–F) *p* values were calculated using two-tailed, unpaired t-tests.

DISCUSSION

The discovery of functional noncoding loci and subsequent efforts to uncover their functions has led to new insights in a range of pathophysiological contexts. Here, we present a systematic exploration of lncRNA loci in myeloid leukemia, starting from HSPC/AML signatures from a patient cohort, proceeding through screens and extensive functional studies, and concluding with experiments in primary cells. We describe a previously uncharacterized lncRNA locus that is required by myeloid leukemia cells from various cytogenetic and mutational backgrounds: *MYNRL15*. By integrating several lines of evidence, we implicate elements embedded in the *MYNRL15* locus in the RNA-independent regulation of cancer dependency pathways and long-range chromatin architecture. To our knowledge, this is the first functionally relevant RNA-independent lncRNA locus reported in myeloid leukemia. Notably, *MYNRL15* perturbation showed strong anti-leukemic effects in primary AML cells of different genetic backgrounds, implying therapeutic interest, which we validated with proof-of-principle *in vivo* experiments using AML PDXs.

In our study, *MYNRL15* perturbation resulted in the formation of a long-range chromatin interaction and downregulation of cancer dependency genes, including several in the gained interaction region. The range of the gained interaction (12–15 Mb away from the *MYNRL15* locus) is far greater than what is described in the literature for topologically associating domain (TAD) fusion[29–31] or enhancer-promoter loops.[32] It is unclear what large-scale chromatin re-organization mechanism could be responsible for bringing the *MYNRL15* locus into contact with this distal site. However, we identified 9 potential transcription factors that may mediate the interaction, based on their occupancy of *MYNRL15*'s C1/C2 regions and the distal interaction sites.

We note that, while there is considerable overlap between enhancer RNA (eRNA) and lncRNA annotations,[14] and while some of our data support a local enhancer-like function for *MYNRL15*, we did not find evidence for locally driven phenotypes or RNA function. We cannot completely exclude the possibility that *MYNRL15* may act as an enhancer on nearby genes, but based on integrative differential expression and leukemia dependency analyses, it seems unlikely that these local transcriptional effects are responsible for the strong anti-leukemic phenotype triggered by *MYNRL15* perturbation. The long-range architectural changes and associated downregulation of leukemia dependency genes at the distal interaction sites represent our most compelling lead on candidate targets of the *MYNRL15* locus.

Given the attenuated impact of *MYNRL15* perturbation on normal HSPCs compared to AML cells, we speculate that distal connectivity may be the native conformation of the locus that is lost during leukemic transformation; thus, re-introducing it would selectively impair leukemic cells. The oncogenic rewiring of 3D chromatin architecture through mutations and structural variants has been reported in cancer.[31,33–36] However, it is unlikely that genetic alteration underlies *MYNRL15*'s role in leukemia, since the locus is required by cells from varied cytogenetic and mutational backgrounds. We speculate instead that *MYNRL15* may be involved in unifying leukemic genome organization signatures similar to the phenomenon of stemness-related expression and epigenetic signatures.[16,37,38] Recent studies have begun to implicate aspects of chromatin architecture in cell state transitions during hematopoiesis[39–43] and in the maintenance of leukemic transcription programs.[44–47] Future studies may further reveal leukemic 3D genome organization signatures that underpin general oncogenic behaviors, irrespective of mutational drivers. Such signatures may be ideal targets for the development of cancer-specific therapies, especially if they are common across different genetic subtypes.

Limitations of the study

In this study, we implicate *MYNRL15* in the RNA-independent regulation of chromatin architecture and cancer dependency pathways in myeloid leukemia. Although we observed gained long-range interactions following *MYNRL15* perturbation, and downregulation of key genes near the gained interaction sites, the exact mechanism remains elusive. As discussed previously, while we cannot completely exclude a local enhancer-like role for *MYNRL15*, we suspect that the long-range chromatin interaction involving *IMP3*, *WDR61*, *COMMD4*, etc. is the most relevant part of its leukemia dependency. Further investigation into genome-wide chromatin conformation (e.g., using Hi-C) or co-localization assays (e.g., FISH) may shed light on what large-scale reorganization occurs upon *MYNRL15* perturbation to bring the locus into contact with the distal interaction sites. In addition, pulldown, immunoprecipitation, and/or proteomic studies may help identify the transcription factor(s) that mediate this interaction.

STAR★METHODS

Detailed methods are provided in the online version of this paper and include the following:

- KEY RESOURCES TABLE
- RESOURCE AVAILABILITY
  - Lead contact
  - Materials availability
  - Data and code availability
- EXPERIMENTAL MODEL AND STUDY PARTICIPANT DETAILS
  - Animal studies
  - Human participants
  - Cells and cell culture
- METHOD DETAILS
  - Lentiviral vectors
  - Lentiviruses

- LNA-GapmeRs
- CRISPR library design
- CRISPR library cloning and screening
- Fluorescence-based proliferation assays
- Flow cytometry and cell sorting
- Hematopoietic assays
- Animal experiments
- RNA sequencing
- Next generation Capture-C
- Dual luciferase assays
- Quantitative real-time PCR
- CRISPR-Cas9 indel and excision validation
- TCGA/TARGET

- QUANTIFICATIONS AND STATISTICAL ANALYSIS

SUPPLEMENTAL INFORMATION

Supplemental information can be found online at https://doi.org/10.1016/j.isci.2023.107844.

ACKNOWLEDGMENTS

We thank D. Downes and J. R. Hughes (MRC Weatherall Institute, Oxford) for providing the NG Capture-C protocol and consulting on experimental design. We also thank A. Schwarzer, F. F. Adams (Hannover Medical School), V. Amstislavskiy (Max Planck Institute for Molecular Genetics), and J. L. Mateo (University of Oviedo) for bioinformatics guidance, and A. Kovacsovics (Max Planck Institute for Molecular Genetics), A. Navarrete Santos, L. Gack, K. Huke, K. Menge, C. Beyer (Martin Luther University Halle-Wittenberg), and F. Kalensee (Goethe University Frankfurt) for technical assistance.

This work was supported by the following funding: J.H.K. – European Research Council Horizon 2020 program (#714226), *Hilfe für krebskranke Kinder Frankfurt e.V.,* St. Baldrick's Robert Arceci Innovations Award; D.H. – German Cancer Aid (#111743); M.N. – Hannover Biomedical Research School stipend.

Illustrations and the graphical abstract were created with BioRender.com.

AUTHOR CONTRIBUTIONS

M.N., L.V., H.I., R.B., R.W., L.S. O.A., and D.B. performed experiments and analyzed the results. M.N., K.S., E.R., and M.L.Y. conducted bioinformatic analyses. D.R. and M.H. provided patient samples. D.H. and J.H.K. designed and supervised the study. M.N., M.W.V., D.H., and J.H.K. crafted the manuscript. All authors revised and approved the manuscript.

DECLARATION OF INTERESTS

J.H.K. has advisory roles for Bluebird Bio, Boehringer Ingelheim, Novartis, Roche and Jazz Pharmaceuticals. D.R. has advisory roles for Celgene Corporation, Novartis, Bluebird Bio, Janssen, and receives research funding from CLS Behring and Roche. M.H. receives research funding from Abbvie, Agios, Astellas, BergenBio, Bristol-Myers Squibb, Glycostem, Jazz Pharmaceuticals, Karyopharm, Loxo Oncology, and PinotBio, has received honoraria from Novartis, Pfizer, Jazz Pharmaceuticals, Janssen, Certara, and Sobi, and has advisory roles for Abbvie, BMS, Glycostem, Servier, PinotBio, Amgen, Pfizer, and LabDelbert.

Received: October 19, 2022
Revised: May 2, 2023
Accepted: September 4, 2023
Published: September 7, 2023

REFERENCES

1. ENCODE Project Consortium, Moore, J.E., Purcaro, M.J., Pratt, H.E., Epstein, C.B., Shoresh, N., Adrian, J., Kawli, T., Davis, C.A., Dobin, A., et al. (2020). Expanded encyclopaedias of DNA elements in the human and mouse genomes. Nature *583*, 699–710. https://doi.org/10.1038/s41586-020-2493-4.
2. Slack, F.J., and Chinnaiyan, A.M. (2019). The Role of Non-coding RNAs in Oncology. Cell *179*, 1033–1055. https://doi.org/10.1016/j.cell.2019.10.017.
3. Zhou, S., Treloar, A.E., and Lupien, M. (2016). Emergence of the Noncoding Cancer Genome: A Target of Genetic and Epigenetic Alterations. Cancer Discov. *6*, 1215–1229. https://doi.org/10.1158/2159-8290.CD-16-0745.
4. Short, N.J., Rytting, M.E., and Cortes, J.E. (2018). Acute myeloid leukaemia. Lancet *392*, 593–606. https://doi.org/10.1016/S0140-6736(18)31041-9.
5. Garzon, R., Volinia, S., Papaioannou, D., Nicolet, D., Kohlschmidt, J., Yan, P.S., Mrózek, K., Bucci, D., Carroll, A.J., Baer, M.R., et al. (2014). Expression and prognostic impact of lncRNAs in acute myeloid leukemia. Proc. Natl. Acad. Sci. USA *111*, 18679–18684. https://doi.org/10.1073/pnas.1422050112.

6. Schwarzer, A., Emmrich, S., Schmidt, F., Beck, D., Ng, M., Reimer, C., Adams, F.F., Grasedieck, S., Witte, D., Käbler, S., et al. (2017). The non-coding RNA landscape of human hematopoiesis and leukemia. Nat. Commun. *8*, 218. https://doi.org/10.1038/s41467-017-00212-4.
7. Beck, D., Thoms, J.A.I., Palu, C., Herold, T., Shah, A., Olivier, J., Boelen, L., Huang, Y., Chacon, D., Brown, A., et al. (2018). A four-gene LincRNA expression signature predicts risk in multiple cohorts of acute myeloid leukemia patients. Leukemia *32*, 263–272. https://doi.org/10.1038/leu.2017.210.
8. Bill, M., Papaioannou, D., Karunasiri, M., Kohlschmidt, J., Pepe, F., Walker, C.J., Walker, A.E., Brannan, Z., Pathmanathan, A., Zhang, X., et al. (2019). Expression and functional relevance of long non-coding RNAs in acute myeloid leukemia stem cells. Leukemia *33*, 2169–2182. https://doi.org/10.1038/s41375-019-0429-5.
9. Kopp, F., and Mendell, J.T. (2018). Functional Classification and Experimental Dissection of Long Noncoding RNAs. Cell *172*, 393–407. https://doi.org/10.1016/j.cell.2018.01.011.
10. Ng, M., Heckl, D., and Klusmann, J.H. (2019). The Regulatory Roles of Long Noncoding RNAs in Acute Myeloid Leukemia. Front. Oncol. *9*, 570. https://doi.org/10.3389/fonc.2019.00570.
11. Papaioannou, D., Petri, A., Dovey, O.M., Terreri, S., Wang, E., Collins, F.A., Woodward, L.A., Walker, A.E., Nicolet, D., Pepe, F., et al. (2019). The long non-coding RNA HOXB-AS3 regulates ribosomal RNA transcription in NPM1-mutated acute myeloid leukemia. Nat. Commun. *10*, 5351. https://doi.org/10.1038/s41467-019-13259-2.
12. Zhu, G., Luo, H., Feng, Y., Guryanova, O.A., Xu, J., Chen, S., Lai, Q., Sharma, A., Xu, B., Zhao, Z., et al. (2021). HOXBLINC long non-coding RNA activation promotes leukemogenesis in NPM1-mutant acute myeloid leukemia. Nat. Commun. *12*, 1956. https://doi.org/10.1038/s41467-021-22095-2.
13. Luo, H., Zhu, G., Eshelman, M.A., Fung, T.K., Lai, Q., Wang, F., Zeisig, B.B., Lesperance, J., Ma, X., Chen, S., et al. (2022). HOTTIP-dependent R-loop formation regulates CTCF boundary activity and TAD integrity in leukemia. Mol. Cell *82*, 833–851.e11. https://doi.org/10.1016/j.molcel.2022.01.014.
14. Sartorelli, V., and Lauberth, S.M. (2020). Enhancer RNAs are an important regulatory layer of the epigenome. Nat. Struct. Mol. Biol. *27*, 521–528. https://doi.org/10.1038/s41594-020-0446-0.
15. Cho, S.W., Xu, J., Sun, R., Mumbach, M.R., Carter, A.C., Chen, Y.G., Yost, K.E., Kim, J., He, J., Nevins, S.A., et al. (2018). Promoter of lncRNA Gene PVT1 Is a Tumor-Suppressor DNA Boundary Element. Cell *173*, 1398–1412.e22. https://doi.org/10.1016/j.cell.2018.03.068.
16. Eppert, K., Takenaka, K., Lechman, E.R., Waldron, L., Nilsson, B., van Galen, P., Metzeler, K.H., Poeppl, A., Ling, V., Beyene, J., et al. (2011). Stem cell gene expression programs influence clinical outcome in human leukemia. Nat. Med. *17*, 1086–1093. https://doi.org/10.1038/nm.2415.
17. Krivtsov, A.V., Figueroa, M.E., Sinha, A.U., Stubbs, M.C., Feng, Z., Valk, P.J.M., Delwel, R., Döhner, K., Bullinger, L., Kung, A.L., et al. (2013). Cell of origin determines clinically relevant subtypes of MLL-rearranged AML. Leukemia *27*, 852–860. https://doi.org/10.1038/leu.2012.363.
18. Li, W., Xu, H., Xiao, T., Cong, L., Love, M.I., Zhang, F., Irizarry, R.A., Liu, J.S., Brown, M., and Liu, X.S. (2014). MAGeCK enables robust identification of essential genes from genome-scale CRISPR/Cas9 knockout screens. Genome Biol. *15*, 554. https://doi.org/10.1186/s13059-014-0554-4.
19. Liu, S.J., Horlbeck, M.A., Cho, S.W., Birk, H.S., Malatesta, M., He, D., Attenello, F.J., Villalta, J.E., Cho, M.Y., Chen, Y., et al. (2017). CRISPRi-based genome-scale identification of functional long noncoding RNA loci in human cells. Science *355*, aah7111. https://doi.org/10.1126/science.aah7111.
20. Liu, Y., Cao, Z., Wang, Y., Guo, Y., Xu, P., Yuan, P., Liu, Z., He, Y., and Wei, W. (2018). Genome-wide screening for functional long noncoding RNAs in human cells by Cas9 targeting of splice sites. Nat. Biotechnol. *36*, 1203–1210. https://doi.org/10.1038/nbt.4283.
21. Joung, J., Engreitz, J.M., Konermann, S., Abudayyeh, O.O., Verdine, V.K., Aguet, F., Gootenberg, J.S., Sanjana, N.E., Wright, J.B., Fulco, C.P., et al. (2017). Genome-scale activation screen identifies a lncRNA locus regulating a gene neighbourhood. Nature *548*, 343–346. https://doi.org/10.1038/nature23451.
22. Davies, J.O.J., Telenius, J.M., McGowan, S.J., Roberts, N.A., Taylor, S., Higgs, D.R., and Hughes, J.R. (2016). Multiplexed analysis of chromosome conformation at vastly improved sensitivity. Nat. Methods *13*, 74–80. https://doi.org/10.1038/nmeth.3664.
23. Hsieh, T.H.S., Fudenberg, G., Goloborodko, A., and Rando, O.J. (2016). Micro-C XL: assaying chromosome conformation from the nucleosome to the entire genome. Nat. Methods *13*, 1009–1011. https://doi.org/10.1038/nmeth.4025.
24. Tsherniak, A., Vazquez, F., Montgomery, P.G., Weir, B.A., Kryukov, G., Cowley, G.S., Gill, S., Harrington, W.F., Pantel, S., Krill-Burger, J.M., et al. (2017). Defining a Cancer Dependency Map. Cell *170*, 564–576.e16. https://doi.org/10.1016/j.cell.2017.06.010.
25. Granneman, S., Gallagher, J.E.G., Vogelzangs, J., Horstman, W., van Venrooij, W.J., Baserga, S.J., and Pruijn, G.J.M. (2003). The human Imp3 and Imp4 proteins form a ternary complex with hMpp10, which only interacts with the U3 snoRNA in 60-80S ribonucleoprotein complexes. Nucleic Acids Res. *31*, 1877–1887. https://doi.org/10.1093/nar/gkg300.
26. Milne, T.A., Kim, J., Wang, G.G., Stadler, S.C., Basrur, V., Whitcomb, S.J., Wang, Z., Ruthenburg, A.J., Elenitoba-Johnson, K.S.J., Roeder, R.G., and Allis, C.D. (2010). Multiple interactions recruit MLL1 and MLL1 fusion proteins to the HOXA9 locus in leukemogenesis. Mol. Cell *38*, 853–863. https://doi.org/10.1016/j.molcel.2010.05.011.
27. Muntean, A.G., Tan, J., Sitwala, K., Huang, Y., Bronstein, J., Connelly, J.A., Basrur, V., Elenitoba-Johnson, K.S.J., and Hess, J.L. (2010). The PAF complex synergizes with MLL fusion proteins at HOX loci to promote leukemogenesis. Cancer Cell *17*, 609–621. https://doi.org/10.1016/j.ccr.2010.04.012.
28. Saha, N., Ropa, J., Chen, L., Hu, H., Mysliwski, M., Friedman, A., Maillard, I., and Muntean, A.G. (2019). The PAF1c Subunit CDC73 Is Required for Mouse Hematopoietic Stem Cell Maintenance but Displays Leukemia-Specific Gene Regulation. Stem Cell Rep. *12*, 1069–1083. https://doi.org/10.1016/j.stemcr.2019.03.010.
29. Lupiáñez, D.G., Kraft, K., Heinrich, V., Krawitz, P., Brancati, F., Klopocki, E., Horn, D., Kayserili, H., Opitz, J.M., Laxova, R., et al. (2015). Disruptions of topological chromatin domains cause pathogenic rewiring of gene-enhancer interactions. Cell *161*, 1012–1025. https://doi.org/10.1016/j.cell.2015.04.004.
30. Despang, A., Schöpflin, R., Franke, M., Ali, S., Jerković, I., Paliou, C., Chan, W.L., Timmermann, B., Wittler, L., Vingron, M., et al. (2019). Functional dissection of the Sox9-Kcnj2 locus identifies nonessential and instructive roles of TAD architecture. Nat. Genet. *51*, 1263–1271. https://doi.org/10.1038/s41588-019-0466-z.
31. Flavahan, W.A., Drier, Y., Liau, B.B., Gillespie, S.M., Venteicher, A.S., Stemmer-Rachamimov, A.O., Suvà, M.L., and Bernstein, B.E. (2016). Insulator dysfunction and oncogene activation in IDH mutant gliomas. Nature *529*, 110–114. https://doi.org/10.1038/nature16490.
32. Schoenfelder, S., and Fraser, P. (2019). Long-range enhancer-promoter contacts in gene expression control. Nat. Rev. Genet. *20*, 437–455. https://doi.org/10.1038/s41576-019-0128-0.
33. Hnisz, D., Weintraub, A.S., Day, D.S., Valton, A.L., Bak, R.O., Li, C.H., Goldmann, J., Lajoie, B.R., Fan, Z.P., Sigova, A.A., et al. (2016). Activation of proto-oncogenes by disruption of chromosome neighborhoods. Science *351*, 1454–1458. https://doi.org/10.1126/science.aad9024.
34. Akdemir, K.C., Le, V.T., Chandran, S., Li, Y., Verhaak, R.G., Beroukhim, R., Campbell, P.J., Chin, L., Dixon, J.R., Futreal, P.A., et al. (2020). Disruption of chromatin folding domains by somatic genomic rearrangements in human cancer. Nat. Genet. *52*, 294–305. https://doi.org/10.1038/s41588-019-0564-y.
35. Katainen, R., Dave, K., Pitkänen, E., Palin, K., Kivioja, T., Välimäki, N., Gylfe, A.E., Ristolainen, H., Hänninen, U.A., Cajuso, T., et al. (2015). CTCF/cohesin-binding sites are frequently mutated in cancer. Nat. Genet. *47*, 818–821. https://doi.org/10.1038/ng.3335.
36. Gröschel, S., Sanders, M.A., Hoogenboezem, R., de Wit, E., Bouwman, B.A.M., Erpelinck, C., van der Velden, V.H.J., Havermans, M., Avellino, R., van Lom, K., et al. (2014). A single oncogenic enhancer rearrangement causes concomitant EVI1 and GATA2 deregulation in leukemia. Cell *157*, 369–381. https://doi.org/10.1016/j.cell.2014.02.019.
37. Jung, N., Dai, B., Gentles, A.J., Majeti, R., and Feinberg, A.P. (2015). An LSC epigenetic signature is largely mutation independent and implicates the HOXA cluster in AML pathogenesis. Nat. Commun. *6*, 8489. https://doi.org/10.1038/ncomms9489.
38. Zhu, S., Li, W., Liu, J., Chen, C.H., Liao, Q., Xu, P., Xu, H., Xiao, T., Cao, Z., Peng, J., et al. (2016). Genome-scale deletion screening of human long non-coding RNAs using a paired-guide RNA CRISPR-Cas9 library. Nat. Biotechnol. *34*, 1279–1286. https://doi.org/10.1038/nbt.3715.
39. Chen, C., Yu, W., Tober, J., Gao, P., He, B., Lee, K., Trieu, T., Blobel, G.A., Speck, N.A., and Tan, K. (2019). Spatial Genome Re-organization between Fetal and Adult Hematopoietic Stem Cells. Cell Rep. *29*, 4200–4211.e7. https://doi.org/10.1016/j.celrep.2019.11.065.
40. Qi, Q., Cheng, L., Tang, X., He, Y., Li, Y., Yee, T., Shrestha, D., Feng, R., Xu, P., Zhou, X.,

et al. (2021). Dynamic CTCF binding directly mediates interactions among cis-regulatory elements essential for hematopoiesis. Blood *137*, 1327–1339. https://doi.org/10.1182/blood.2020005780.

41. Takayama, N., Murison, A., Takayanagi, S.I., Arlidge, C., Zhou, S., Garcia-Prat, L., Chan-Seng-Yue, M., Zandi, S., Gan, O.I., Boutzen, H., et al. (2021). The Transition from Quiescent to Activated States in Human Hematopoietic Stem Cells Is Governed by Dynamic 3D Genome Reorganization. Cell Stem Cell *28*, 488–501.e10. https://doi.org/10.1016/j.stem.2020.11.001.
42. Hu, G., Cui, K., Fang, D., Hirose, S., Wang, X., Wangsa, D., Jin, W., Ried, T., Liu, P., Zhu, J., et al. (2018). Transformation of Accessible Chromatin and 3D Nucleome Underlies Lineage Commitment of Early T Cells. Immunity *48*, 227–242.e8. https://doi.org/10.1016/j.immuni.2018.01.013.
43. Zhang, C., Xu, Z., Yang, S., Sun, G., Jia, L., Zheng, Z., Gu, Q., Tao, W., Cheng, T., Li, C., and Cheng, H. (2020). tagHi-C Reveals 3D Chromatin Architecture Dynamics during Mouse Hematopoiesis. Cell Rep. *32*, 108206. https://doi.org/10.1016/j.celrep.2020.108206.
44. Kloetgen, A., Thandapani, P., Ntziachristos, P., Ghebrechristos, Y., Nomikou, S., Lazaris, C., Chen, X., Hu, H., Bakogianni, S., Wang, J., et al. (2020). Three-dimensional chromatin landscapes in T cell acute lymphoblastic leukemia. Nat. Genet. *52*, 388–400. https://doi.org/10.1038/s41588-020-0602-9.
45. Luo, H., Wang, F., Zha, J., Li, H., Yan, B., Du, Q., Yang, F., Sobh, A., Vulpe, C., Drusbosky, L., et al. (2018). CTCF boundary remodels chromatin domain and drives aberrant HOX gene transcription in acute myeloid leukemia. Blood *132*, 837–848. https://doi.org/10.1182/blood-2017-11-814319.
46. Vilarrasa-Blasi, R., Soler-Vila, P., Verdaguer-Dot, N., Russiñol, N., Di Stefano, M., Chapaprieta, V., Clot, G., Farabella, I., Cuscó, P., Kulis, M., et al. (2021). Dynamics of genome architecture and chromatin function during human B cell differentiation and neoplastic transformation. Nat. Commun. *12*, 651. https://doi.org/10.1038/s41467-020-20849-y.
47. Xu, J., Song, F., Lyu, H., Kobayashi, M., Zhang, B., Zhao, Z., Hou, Y., Wang, X., Luan, Y., Jia, B., et al. (2022). Subtype-specific 3D genome alteration in acute myeloid leukaemia. Nature *611*, 387–398. https://doi.org/10.1038/s41586-022-05365-x.
48. Reimer, J., Knöß, S., Labuhn, M., Charpentier, E.M., Göhring, G., Schlegelberger, B., Klusmann, J.H., and Heckl, D. (2017). CRISPR-Cas9-induced t(11;19)/MLL-ENL translocations initiate leukemia in human hematopoietic progenitor cells *in vivo*. Haematologica *102*, 1558–1566. https://doi.org/10.3324/haematol.2017.
49. Labuhn, M., Adams, F.F., Ng, M., Knoess, S., Schambach, A., Charpentier, E.M., Schwarzer, A., Mateo, J.L., Klusmann, J.H., and Heckl, D. (2018). Refined sgRNA efficacy prediction improves large- and small-scale CRISPR-Cas9 applications. Nucleic Acids Res. *46*, 1375–1385. https://doi.org/10.1093/nar/gkx1268.
50. Alejo-Valle, O., Weigert, K., Bhayadia, R., Ng, M., Issa, H., Beyer, C., Emmrich, S., Schuschel, K., Ihling, C., Sinz, A., et al. (2022). The megakaryocytic transcription factor ARID3A suppresses leukemia pathogenesis. Blood *139*, 651–665. https://doi.org/10.1182/blood.2021012231.
51. Al-Kershi, S., Bhayadia, R., Ng, M., Verboon, L., Emmrich, S., Gack, L., Schwarzer, A., Strowig, T., Heckl, D., and Klusmann, J.H. (2019). The stem cell-specific long noncoding RNA HOXA10-AS in the pathogenesis of KMT2A-rearranged leukemia. Blood Adv. *3*, 4252–4263. https://doi.org/10.1182/bloodadvances.2019032029.
52. Heckl, D., Kowalczyk, M.S., Yudovich, D., Belizaire, R., Puram, R.V., McConkey, M.E., Thielke, A., Aster, J.C., Regev, A., and Ebert, B.L. (2014). Generation of mouse models of myeloid malignancy with combinatorial genetic lesions using CRISPR-Cas9 genome editing. Nat. Biotechnol. *32*, 941–946. https://doi.org/10.1038/nbt.2951.
53. Meers, M.P., Bryson, T.D., Henikoff, J.G., and Henikoff, S. (2019). Improved CUT&RUN chromatin profiling tools. Elife *8*, e46314. https://doi.org/10.7554/eLife.46314.
54. Stemmer, M., Thumberger, T., Del Sol Keyer, M., Wittbrodt, J., and Mateo, J.L. (2015). CCTop: An Intuitive, Flexible and Reliable CRISPR/Cas9 Target Prediction Tool. PLoS One *10*, e0124633. https://doi.org/10.1371/journal.pone.0124633.
55. Concordet, J.P., and Haeussler, M. (2018). CRISPOR: intuitive guide selection for CRISPR/Cas9 genome editing experiments and screens. Nucleic Acids Res. *46*, W242–W245. https://doi.org/10.1093/nar/gky354.
56. Brinkman, E.K., Chen, T., Amendola, M., and van Steensel, B. (2014). Easy quantitative assessment of genome editing by sequence trace decomposition. Nucleic Acids Res. *42*, e168. https://doi.org/10.1093/nar/gku936.
57. Adams, F.F., Heckl, D., Hoffmann, T., Talbot, S.R., Kloos, A., Thol, F., Heuser, M., Zuber, J., Schambach, A., and Schwarzer, A. (2017). An optimized lentiviral vector system for conditional RNAi and efficient cloning of microRNA embedded short hairpin RNA libraries. Biomaterials *139*, 102–115. https://doi.org/10.1016/j.biomaterials.2017.05.032.
58. Love, M.I., Huber, W., and Anders, S. (2014). Moderated estimation of fold change and dispersion for RNA-seq data with DESeq2. Genome Biol. *15*, 550. https://doi.org/10.1186/s13059-014-0550-8.
59. Leek, J.T., Johnson, W.E., Parker, H.S., Jaffe, A.E., and Storey, J.D. (2012). The sva package for removing batch effects and other unwanted variation in high-throughput experiments. Bioinformatics *28*, 882–883. https://doi.org/10.1093/bioinformatics/bts034.
60. van der Maaten, L., and Hinton, G. (2008). Visualizing high-dimensional data using t-SNE. J. Mach. Learn. Res. *9*, 2579–2605.
61. Subramanian, A., Tamayo, P., Mootha, V.K., Mukherjee, S., Ebert, B.L., Gillette, M.A., Paulovich, A., Pomeroy, S.L., Golub, T.R., Lander, E.S., and Mesirov, J.P. (2005). Gene set enrichment analysis: a knowledge-based approach for interpreting genome-wide expression profiles. Proc. Natl. Acad. Sci. USA *102*, 15545–15550. https://doi.org/10.1073/pnas.0506580102.
62. Liberzon, A., Birger, C., Thorvaldsdóttir, H., Ghandi, M., Mesirov, J.P., and Tamayo, P. (2015). The Molecular Signatures Database (MSigDB) hallmark gene set collection. Cell Syst. *1*, 417–425. https://doi.org/10.1016/j.cels.2015.12.004.
63. Sherman, B.T., Hao, M., Qiu, J., Jiao, X., Baseler, M.W., Lane, H.C., Imamichi, T., and Chang, W. (2022). DAVID: a web server for functional enrichment analysis and functional annotation of gene lists (2021 update). Nucleic Acids Res. *50*, W216–W221. https://doi.org/10.1093/nar/gkac194.
64. Hughes, J.R., Roberts, N., McGowan, S., Hay, D., Giannoulatou, E., Lynch, M., De Gobbi, M., Taylor, S., Gibbons, R., and Higgs, D.R. (2014). Analysis of hundreds of cis-regulatory landscapes at high resolution in a single, high-throughput experiment. Nat. Genet. *46*, 205–212. https://doi.org/10.1038/ng.2871.
65. Buckle, A., Gilbert, N., Marenduzzo, D., and Brackley, C.A. (2019). capC-MAP: software for analysis of Capture-C data. Bioinformatics *35*, 4773–4775. https://doi.org/10.1093/bioinformatics/btz480.
66. Robinson, J.T., Thorvaldsdóttir, H., Winckler, W., Guttman, M., Lander, E.S., Getz, G., and Mesirov, J.P. (2011). Integrative genomics viewer. Nat. Biotechnol. *29*, 24–26. https://doi.org/10.1038/nbt.1754.
67. Kent, W.J., Sugnet, C.W., Furey, T.S., Roskin, K.M., Pringle, T.H., Zahler, A.M., and Haussler, D. (2002). The human genome browser at UCSC. Genome Res. *12*, 996–1006. https://doi.org/10.1101/gr.229102.
68. Emmrich, S., Rasche, M., Schöning, J., Reimer, C., Keihani, S., Maroz, A., Xie, Y., Li, Z., Schambach, A., Reinhardt, D., and Klusmann, J.H. (2014). miR-99a/100∼125b tricistrons regulate hematopoietic stem and progenitor cell homeostasis by shifting the balance between TGFbeta and Wnt signaling. Genes Dev. *28*, 858–874. https://doi.org/10.1101/gad.233791.113.
69. Stein, C.A., Hansen, J.B., Lai, J., Wu, S., Voskresenskiy, A., Høg, A., Worm, J., Hedtjärn, M., Souleimanian, N., Miller, P., et al. (2010). Efficient gene silencing by delivery of locked nucleic acid antisense oligonucleotides, unassisted by transfection reagents. Nucleic Acids Res. *38*, e3. https://doi.org/10.1093/nar/gkp841.
70. Harrow, J., Frankish, A., Gonzalez, J.M., Tapanari, E., Diekhans, M., Kokocinski, F., Aken, B.L., Barrell, D., Zadissa, A., Searle, S., et al. (2012). GENCODE: the reference human genome annotation for The ENCODE Project. Genome Res. *22*, 1760–1774. https://doi.org/10.1101/gr.135350.111.
71. Volders, P.J., Verheggen, K., Menschaert, G., Vandepoele, K., Martens, L., Vandesompele, J., and Mestdagh, P. (2015). An update on LNCipedia: a database for annotated human lncRNA sequences. Nucleic Acids Res. *43*, 4363–4364. https://doi.org/10.1093/nar/gkv295.
72. Zhao, Y., Li, H., Fang, S., Kang, Y., Wu, W., Hao, Y., Li, Z., Bu, D., Sun, N., Zhang, M.Q., and Chen, R. (2016). NONCODE 2016: an informative and valuable data source of long non-coding RNAs. Nucleic Acids Res. *44*, D203–D208. https://doi.org/10.1093/nar/gkv1252.
73. Gilbert, L.A., Horlbeck, M.A., Adamson, B., Villalta, J.E., Chen, Y., Whitehead, E.H., Guimaraes, C., Panning, B., Ploegh, H.L., Bassik, M.C., et al. (2014). Genome-Scale CRISPR-Mediated Control of Gene Repression and Activation. Cell *159*, 647–661. https://doi.org/10.1016/j.cell.2014.09.029.
74. Bhayadia, R., Krowiorz, K., Haetscher, N., Jammal, R., Emmrich, S., Obulkasim, A., Fiedler, J., Schwarzer, A., Rouhi, A., Heuser, M., et al. (2018). Endogenous Tumor Suppressor microRNA-193b: Therapeutic and Prognostic Value in Acute Myeloid Leukemia. J. Clin. Oncol. *36*, 1007–1016. https://doi.org/10.1200/JCO.2017.75.2204.

75. Kim, D., Paggi, J.M., Park, C., Bennett, C., and Salzberg, S.L. (2019). Graph-based genome alignment and genotyping with HISAT2 and HISAT-genotype. Nat. Biotechnol. *37*, 907–915. https://doi.org/10.1038/s41587-019-0201-4.
76. Liao, Y., Smyth, G.K., and Shi, W. (2014). featureCounts: an efficient general purpose program for assigning sequence reads to genomic features. Bioinformatics *30*, 923–930. https://doi.org/10.1093/bioinformatics/btt656.
77. Huang, D.W., Sherman, B.T., and Lempicki, R.A. (2009). Systematic and integrative analysis of large gene lists using DAVID bioinformatics resources. Nat. Protoc. *4*, 44–57. https://doi.org/10.1038/nprot.2008.211.
78. Knight, P.A., and Ruiz, D. (2012). A fast algorithm for matrix balancing. IMA J. Numer. Anal. *33*, 1029–1047. https://doi.org/10.1093/imanum/drs019.
79. Krietenstein, N., Abraham, S., Venev, S.V., Abdennur, N., Gibcus, J., Hsieh, T.H.S., Parsi, K.M., Yang, L., Maehr, R., Mirny, L.A., et al. (2020). Ultrastructural Details of Mammalian Chromosome Architecture. Mol. Cell *78*, 554–565.e7. https://doi.org/10.1016/j.molcel.2020.03.003.
80. Rao, S.S.P., Huntley, M.H., Durand, N.C., Stamenova, E.K., Bochkov, I.D., Robinson, J.T., Sanborn, A.L., Machol, I., Omer, A.D., Lander, E.S., and Aiden, E.L. (2014). A 3D map of the human genome at kilobase resolution reveals principles of chromatin looping. Cell *159*, 1665–1680. https://doi.org/10.1016/j.cell.2014.11.021.
81. Cabianca, D.S., Casa, V., Bodega, B., Xynos, A., Ginelli, E., Tanaka, Y., and Gabellini, D. (2012). A long ncRNA links copy number variation to a polycomb/trithorax epigenetic switch in FSHD muscular dystrophy. Cell *149*, 819–831. https://doi.org/10.1016/j.cell.2012.03.035.
82. Cancer Genome Atlas Research Network, Ley, T.J., Miller, C., Ding, L., Raphael, B.J., Mungall, A.J., Robertson, A.G., Hoadley, K., Triche, T.J., Jr., Laird, P.W., et al. (2013). Genomic and epigenomic landscapes of adult de novo acute myeloid leukemia. N. Engl. J. Med. *368*, 2059–2074. https://doi.org/10.1056/NEJMoa1301689.
83. Bolouri, H., Farrar, J.E., Triche, T., Jr., Ries, R.E., Lim, E.L., Alonzo, T.A., Ma, Y., Moore, R., Mungall, A.J., Marra, M.A., et al. (2018). The molecular landscape of pediatric acute myeloid leukemia reveals recurrent structural alterations and age-specific mutational interactions. Nat. Med. *24*, 103–112. https://doi.org/10.1038/nm.4439.

STAR★METHODS

KEY RESOURCES TABLE

REAGENT or RESOURCE	SOURCE	IDENTIFIER
Antibodies		
Anti-human CD45-FITC (clone J33)	Beckman Coulter	Cat# A07782; RRID:AB_10645157
Bacterial and virus strains		
XL1-Blue supercompetent cells	Agilent	Cat# 200236
Subcloning efficiency DH5a competent cells	Invitrogen	Cat# 18265017
Biological samples		
Healthy CD34$^+$ HSPCs	This paper	N/A
Patient derived xenografts (Table S5)	This paper	N/A
Chemicals, peptides, and recombinant proteins		
Recombinant human SCF	Peprotech	Cat# 300-07
Recombinant human FLT3L	Peprotech	Cat# 300-19
Recombinant human IL-3	Peprotech	Cat# 200-03
Recombinant human IL-6	Peprotech	Cat# 200-06
Recombinant human TPO	Peprotech	Cat# 300-18
Recombinant human GM-CSF	Peprotech	Cat# 300-03
StemRegenin 1	STEMCELL	Cat# 72344
UM171	STEMCELL	Cat# 72914
RetroNectin® recombinant human fibronectin fragment	TaKaRa Bio	Cat# T100B
Lenti-X™ concentrator	TaKaRa Bio	Cat# 631231
Polybrene	Sigma Aldrich	Cat# TR-1003-G
Critical commercial assays		
Plasmid maxi kit	Qiagen	Cat# 12163
QIAamp DNA blood mini kit	Qiagen	Cat# 51104
NEBNext® high-fidelity PCR master mix	New England Biolabs	Cat# M0541L
Human methylcellulose complete media	R&D Systems	Cat# HSC003
Dual-luciferase® reporter assay system	Promega	Cat# E1910
High-capacity cDNA reverse transcription kit	Applied Biosystems	Cat# 4368814
SYBR™ select master mix	Applied Biosystems	Cat# 4472908
Deposited data		
Raw and processed RNA-seq, Capture-C data	This paper	GEO: GSE172240
Raw amplicon sequence data from CRISPR screens	This paper	ENA: PRJEB44308, PRJEB44320
Experimental models: Cell lines		
HEK293T	DSMZ	DSMZ# ACC 635; RRID:CVCL_0063
K562	DSMZ	DSMZ# ACC 10; RRID:CVCL_0004
ML-2	DSMZ	DSMZ# ACC 15; RRID:CVCL_1418
M-07E	DSMZ	DSMZ# ACC 104; RRID:CVCL_2106
KASUMI-1	DSMZ	DSMZ# ACC 220; RRID:CVCL_0589

(*Continued on next page*)

Continued

REAGENT or RESOURCE	SOURCE	IDENTIFIER
NOMO-1	DSMZ	DSMZ# ACC 542; RRID:CVCL_1609
SKNO-1	DSMZ	DSMZ# ACC 690; RRID:CVCL_2196
OCI-AML3	DSMZ	DSMZ# ACC 582; RRID:CVCL_1844
TF-1	DSMZ	DSMZ# ACC 334; RRID:CVCL_0559
NB-4	DSMZ	DSMZ# ACC 207; RRID:CVCL_0005
Experimental models: Organisms/strains		
Mus musculus: NOD.Cg-Prkdc^{scid} Il2rgtm^{1Wjl}/SzJ	Charles River Laboratories	RRID:IMSR_JAX:005557
Oligonucleotides		
sgRNA library sequences (Tables S1–S3)	This paper	N/A
sgRNA, shRNA, LNA-gapmeR sequences (Table S6)	This paper	N/A
PCR and qPCR primers (Table S6)	This paper	N/A
Capture-C probes (Table S6)	This paper	N/A
Negative control B LNA-gapmeR	Qiagen	Cat# 339515
QuantiTect® primer assay for *IMP3*	Qiagen	Cat# QT00232330
QuantiTect® primer assay for *WDR61*	Qiagen	Cat# QT00083776
Recombinant DNA		
psPAX2	N/A	Addgene# 12260
pMD2.G	N/A	Addgene# 12259
SGL40C.EFS.dTomato	Reimer et al.[48]	Addgene# 89395
SGL40C.EFS.E2Crimson	Labuhn et al.[49]	Addgene# 100894
SGL40C.mU6.EFS.RFP657	This paper	Addgene# 207866
SIN40C.SFFV.eGFP.miR30n	Alejo-Valle et al.[50]	Addgene# 169278
LBid.lnc.GFP	Al-Kershi et al.[51]	N/A
L40C-CRISPR.EFS.mNeon	Reimer et al.[48]	Addgene# 69146
pLKO5d.SFFV.dCas9-KRAB.P2A.BSD	Schwarzer et al.[6]	Addgene# 90332
pLKO5d.EFS.SpCas9.P2A.BSD	Heckl et al.[52]	Addgene# 57821
SIN40C.SFFV.dCas9-KRAB.P2A.m.Neon	This paper	Addgene# 170482
SGL.EFS.tBFP	This paper	Addgene# 173915
pAG/MNase	Meers et al.[53]	Addgene# 123461
pGL4.23	Promega	Cat# E8411
Software and algorithms		
GraphPad Prism	GraphPad	https://www.graphpad.com/scientific-software/prism/; RRID:SCR_002798
FlowJo	BD Biosciences	https://www.flowjo.com/solutions/flowjo; RRID:SCR_008520
Kaluza	Beckman Coulter	https://www.beckman.com/flow-cytometry/software/kaluza; RRID:SCR_016182
CCTop	Stemmer et al.[54]	https://cctop.cos.uni-heidelberg.de/; RRID:SCR_016890
CRISPOR	Concordet and Haeussler,[55]	http://crispor.tefor.net/; RRID:SCR_015935
MAGeCK	Li et al.[18]	https://sourceforge.net/p/mageck/wiki/
TIDE	Brinkman et al.[56]	http://shinyapps.datacurators.nl/tide/
miR-N	Adams et al.[57]	http://shinyapps.datacurators.nl/tide/
R	R project	https://www.r-project.org/about.html; RRID:SCR_001905

(*Continued on next page*)

Continued

REAGENT or RESOURCE	SOURCE	IDENTIFIER
R: DESeq2	Love et al.[58]	https://bioconductor.org/packages/release/bioc/html/DESeq2.html; RRID:SCR_015687
R: sva	Leek et al.[59]	https://bioconductor.org/packages/release/bioc/html/sva.html; RRID:SCR_012836
R: Rtsne	van der Maaten and Hinton,[60]	https://cran.r-project.org/web/packages/Rtsne/index.html; RRID:SCR_016342
GSEA	Subramanian et al.[61]	https://www.gsea-msigdb.org/gsea/index.jsp; RRID:SCR_003199
MSigDB	Liberzon et al.[62]	https://www.gsea-msigdb.org/gsea/msigdb/index.jsp; RRID:SCR_016863
DAVID	Sherman et al.[63]	https://david.ncifcrf.gov/home.jsp
CapSequm2	Hughes et al.,[64]	https://capsequm.molbiol.ox.ac.uk/cgi-bin/CapSequm.cgi
capC-MAP	Buckle et al.,[65]	https://capc-map.readthedocs.io/en/latest/
IGV	Robinson et al.[66]	https://software.broadinstitute.org/software/igv/; RRID:SCR_011793
UCSC genome browser	Kent et al.[67]	https://genome.ucsc.edu/; RRID:SCR_005780
Other		
Ensembl gene, transcript, CDS annotations	Ensembl	http://www.ensembl.org/index.html; RRID:SCR_002344
K562 ChIP-seq data: H3K4Me3, H3K4Me1, H3K27Ac, CTCF, SMC3, AGO1, BHLHE40, E2F6, EGR1, ESRRA, GABPB1, GMEB1, HNRNPLL, IRF1, L3MBTL2, MAX, MNT, NRF1, PHF20, PHF8, PML, PRDM10, RBFOX2, RLF, RNF2, SAP30, TBP, THRA, ZBTB7A, ZNF639	ENCODE	https://www.encodeproject.org/; RRID:SCR_015482; ENCFF767UON, ENCFF759NWD, ENCFF038DDS, ENCFF519CXF, ENCFF175UEE, ENCFF100VYA, ENCFF477JTV, ENCFF533GSH, ENCFF375RDB, ENCFF592GWM, ENCFF700DXR, ENCFF678VPQ, ENCFF662WPN, ENCFF978BBL, ENCFF423LPW, ENCFF618VMC, ENCFF926CRV, ENCFF543STN, ENCFF259HUS, ENCFF952YDR, ENCFF800QDU, ENCFF600HPZ, ENCFF232ASB, ENCFF599CBB, ENCFF349MSP, ENCFF103RHL, ENCFF370YGS, ENCFF309DMZ, ENCFF245LRG, ENCFF404EVY
H1-hESC Micro-C and K562, KBM7, GM12878, NHEK, HUVEC, HMEC, IMR90 Hi-C data	4DN	https://data.4dnucleome.org/; RRID:SCR_016925; 4DNFI2TK7L2F, 4DNESI7DEJTM, 4DNESDEK4IH8, 4DNES3JX38V5, 4DNESECNR4O8, 4DNESHFBC56P, 4DNESIE5R9HS, 4DNES1ZEJNRU
Genome-wide CRISPR screening data	DepMap	https://depmap.org/portal/download
TCGA AML RNA-seq data	TCGA	https://gdc.cancer.gov/access-data
TARGET AML RNA-seq data	TARGET	https://ocg.cancer.gov/programs/target/data-matrix
LncScape expression data	Schwarzer et al.[6]	https://ag-klusmann.shinyapps.io/lncScape/

RESOURCE AVAILABILITY

Lead contact

Further information and requests for resources and reagents should be directed to and will be fulfilled by the lead contact, Jan-Henning Klusmann (jan-henning.klusmann@kgu.de).

Materials availability

All plasmids generated in this study have been deposited to Addgene. Plasmid catalog numbers are listed in the "lentiviral vectors" section of the STAR methods.

Data and code availability

- RNA-seq and Capture-C data generated by this study have been deposited in the Gene Expression Omnibus (GEO) under the accession number GSE172240. Raw sequencing data from the CRISPR screens have been deposited in the European Nucleotide Archive at EMBL-EBI under the accession numbers PRJEB44308 and PRJEB44320. Genome-wide CRISPR-Cas9 screening data were obtained from the DepMap Project[24] portal (https://depmap.org/portal/download). Histone and transcription factor ChIP-seq data from ENCODE, and Micro-C and Hi-C data from the 4D Nucleome Data Portal were used in this study (refer to key resources table for identifiers). RNA-seq data from adult and pediatric AML patients were obtained from TCGA (https://gdc.cancer.gov/access-data) and TARGET (https://ocg.cancer.gov/programs/target/data-matrix), respectively. Microarray data from normal hematopoietic cells and pediatric AML samples were previously generated by our lab[6] (https://ag-klusmann.shinyapps.io/lncScape/).
- This paper used existing analysis algorithms (see STAR methods) and does not report original code.
- Any additional information required to reanalyze the data reported in this paper is available from the lead contacts upon request.

EXPERIMENTAL MODEL AND STUDY PARTICIPANT DETAILS

Animal studies

This study involved animal experiments using NOD.Cg-Prkdc^{scid} Il2rgtm^{1Wjl}/SzJ (NSG) immunodeficient mice (Charles River Laboratories). 8–10 week old female littermates were randomly assigned to experimental groups. The mice were group housed in individual ventilated cages with autoclaved food and water in a pathogen-free environment at the Martin Luther University Halle-Wittenberg. All animal procedures were approved by the state authorities (Landesverwaltungsamt Sachsen-Anhalt).

Human participants

Human CD34$^+$ HSPCs were isolated from mobilized peripheral blood of anonymous healthy donors. AML samples were provided by the Berlin-Frankfurt-Münster Study Group (AML-BFM-SG, Essen Germany) and the Department of Hematology, Hemostasis, Oncology and Stem Cell Transplantation (Hannover Medical School). Informed consent was obtained from all human participants or custodians. Please refer to Table S5 for patient characteristics including sex and age. Information about gender was not collected, and patient characteristics were not provided for the anonymous healthy donors. All investigations were approved by the ethics committee of the Martin Luther University Halle-Wittenberg.

Cells and cell culture

HEK293T cells and the human leukemia cell lines K562, ML-2, M-07E, KASUMI-1, NOMO-1, SKNO-1, OCI-AML3, TF-1, NB-4 were obtained from the German National Resource Center for Biological Material (DSMZ, Braunschweig, Germany) and cultured according to their recommendations. The cells were authenticated by the vendor and no further authentication was performed in the laboratory. All cell lines were routinely tested for mycoplasma contamination. Cell line characteristics including sex and age can be found in Table S5. Culture conditions for primary HSPCs and patient-derived AML cells are described in the "hematopoietic assays" section of the STAR methods.

METHOD DETAILS

Lentiviral vectors

Individual sgRNAs were designed using CCTop[54] (https://cctop.cos.uni-heidelberg.de/), and cloned via BsmBI into the SGL40C.EFS.dTomato (Addgene 89395) or SGL40C.EFS.E2Crimson (100894) backbone. Dual sgRNA vectors were generated by cloning a second promoter (mU6)-sgRNA cassette (207866) into an existing (hU6) sgRNA vector via EcoRI/XhoI. Short hairpin RNAs (shRNAs) for RNA interference were designed using the Adams et al. miR-N tool[57] (https://felixfadams.shinyapps.io/miRN/) and cloned via BsmBI into the SIN40C.SFFV.eGFP.miR30n (169278) backbone. Non-targeting sgRNAs and shRNAs were designed against firefly luciferase. *MYNRL15* cDNAs were expressed from the bidirectional LBid.lnc.GFP[51,68] vector. The L40C-CRISPR.EFS.mNeon (69146) all-in-one system was used on primary cells for *in vitro* hematopoietic assays. Stable cell lines were generated using pLKO5d.SFFV.dCas9-KRAB.P2A.BSD (90332) or pLKO5d.EFS.SpCas9.P2A.BSD (57821). Stable PDXs were made using SIN40C.SFFV.dCas9-KRAB.P2A.m.Neon (170482). The sgRNA libraries

used in this study were expressed from SGL40C.EFS.dTomato (89395; CRISPRi lncRNA and *MYNRL15* tiling) and SGL.EFS.tBFP (173915; gained chromatin interaction region).

Individual sgRNA and shRNA sequences are listed in Table S6. The sgRNA sequences of the three CRISPR libraries in this study are provided in Tables S1, S2, and S4.

Lentiviruses

Lentiviral particles were produced by co-transfecting the expression vector and the packaging plasmids pMD2.G and psPAX2 (Addgene 12259 and 12260 respectively) into HEK293T cells using polyethylenimine (PEI). Viral particles were concentrated via ultracentrifugation, and in the case of all-in-one constructs, were further concentrated using Lenti-X Concentrator reagent (TaKaRa). Transductions were performed in normal cell culture media, in the presence of Polybrene (Sigma-Aldrich).

LNA-GapmeRs

Custom-antisense LNA-GapmeRs targeting the *MYNRL15* transcript were obtained from Qiagen through their in-house design tool. Negative control B (Qiagen 339515) was used as a non-targeting control. Cells were cultured in media containing 2.5 μM LNA-GapmeR for delivery by unassisted uptake.[69] Fresh LNA-GapmeR was added every 2 days to maintain its concentration in the culture media. LNA-GapmeR sequences can be found in Table S6.

CRISPR library design

Guides for CRISPRi-based targeting of HSPC/AML lncRNAs were designed using the stand-alone version of CCTop[54] (https://cctop.cos.uni-heidelberg.de/). In brief, lncRNA genes were annotated using GENCODE v25 (release 03/2016),[70] LNCipedia 4.0 (release 05/2016),[71] and NONCODE v4 (release 01/2014)[72] as previously described,[6] and sgRNAs were selected 0–250 bp downstream of TSSs.[73] Three to nine sgRNAs were selected per gene, depending on the number of different TSSs present in the transcript isoforms and the distance between them. Genes with a single TSS, or with multiple TSSs with high transcript-level support (TSL 1 or 2, according to Ensembl annotations) spaced more than 300 bp apart, were targeted using three sgRNAs per TSS in a 0–150 bp window downstream of the respective TSS. Genes with multiple TSSs in close proximity to each other (spaced $\leq$150 bp apart) were targeted using five sgRNAs in a 0–250 bp window downstream of the first TSS. Guides were prioritized for low off-target binding – a criterion that is built-in to the CCTop tool.

Guides tiling the *MYNRL15* locus were designed by inputting 15 kb of DNA sequence (hg38) symmetrically centered on *MYNRL15* into the CRISPOR[55] (http://crispor.tefor.net/) saturating mutagenesis assistant. To maintain dense tiling of the region (mean coverage: 0.11 sgRNAs per bp), only guides with an MIT specificity score of 0 were excluded.

Guides targeting the 29 protein-coding genes located in the gained distal chromatin interaction region were designed using CCTop[54] (https://cctop.cos.uni-heidelberg.de/). Coding regions (CDS) from Ensembl v102 (release 11/2020) were used as inputs, and where possible, sgRNAs were selected to target most, if not all, protein-coding isoforms. Guides were prioritized for low off-target binding, and those with low predicted on-target efficacies (CRISPRater[49] score<0.4) were excluded.

Due to our usage of SGL40C vectors for lentiviral sgRNA delivery, in which sgRNA transcription is driven from a human U6 promoter, guides containing poly-T stretches (4 or more) were excluded from all libraries, to avoid premature termination of sgRNA transcription mediated by RNA polymerase III. Guides directed against luciferase and the neomycin resistance cassette were used as non-targeting controls, guides targeting *PPP1R12C* and *SLC22A13* were used as nonessential cutting controls, and guides against *MYC*, *MYB*, *ACTB*, *U2AF1*, *RPL9*, and *POL2RA* were used as positive depletion controls. The sgRNA spacer sequences of the three CRISPR libraries used in this study are provided in Tables S1, S2, and S4.

CRISPR library cloning and screening

Library spacer sequences were purchased from Integrated DNA Technologies, pooled, and cloned via BsmBI into one of the following vectors: SGL40C.EFS.dTomato (Addgene 89395; CRISPRi lncRNA and *MYNRL15* tiling), and SGL.EFS.tBFP (173915; gained chromatin interaction region). XL1-Blue supercompetent cells (Agilent 200236) were used for transformation, and subsequently plated on 15 cm LB agar plates containing ampicillin. Colonies were counted from 1 cm^2 areas to ensure sufficient library representation, and then harvested and prepped for plasmid DNA using the QIAGEN Plasmid Maxi Kit. Lentiviral particles were produced as outlined above.

Stable dCas9-KRAB- or Cas9-expressing cell lines were transduced with the sgRNA libraries at an MOI of 0.3, and maintained at 1000-fold representation of the library for 16–18 population doublings. The screens were counted every 2–3 days and split accordingly. Samples were taken at the beginning and end of the screen, to determine differences in sgRNA abundance over time and thereby identify essential genes or regions. Genomic DNA was isolated from these samples via the QIAmp DNA Blood Mini Kit (Qiagen), and the sgRNA cassettes were PCR amplified using the NEBNext High-Fidelity 2x PCR Master Mix (New England Biolabs) and barcoded primers containing the Illumina P5 and P7 adapter sequences as overhangs. The sgRNA amplicons (~300 bp) were gel purified using the GeneJET Gel Extraction Kit (Thermo Fisher Scientific) and sequenced on an Illumina HiSeq 2000 (50 bp single-end reads).

We applied the MAGeCK (model-based analysis of genome-wide CRISPR-Cas9 knockout)[18] pipeline to process raw reads and call AML dependency genes from the CRISPRi lncRNA and gained chromatin interaction region screens. The *MYNRL15* tiling screens were analyzed in R using DESeq2[58] (Bioconductor).

Fluorescence-based proliferation assays

Individual proliferation assays were conducted in stable dCas9-KRAB- or Cas9-expressing cell lines for CRISPR/Cas9 experiments, and in wild-type lines for RNAi experiments. Cells were transduced with individual sgRNA or shRNA perturbation constructs at an efficiency of 40–80%, to attain a mixed population allowing for direct competition between transduced and untransduced cells. These cultures were maintained for up to 20 days, during which fluorescence was tracked every 2–3 days via flow cytometry. Depletion curves were generated by normalizing the percentage of fluorescent (i.e., transduced) cells at each time point to both the initial fluorescence (day 0) and the non-targeting control (sgLUC/shLUC). For the rescue experiment with *MYNRL15* cDNAs, sgRNA-expressing cells were transduced a second time with the cDNA expression constructs. The double-positive population was then tracked by flow cytometry.

Flow cytometry and cell sorting

Flow cytometry data were collected on a CytoFLEX B4-R3-V5 or CytoFLEX S V4-B2-Y4-R3 using CytExpert software (Beckman Coulter). Cell sorting was performed on a FACSAria II using FACSDiva software, or on a FACSMelody using FACSChorus software (BD Biosciences). An anti-human CD45 FITC (Beckman Coulter) antibody was used to analyze xenotransplantation experiments. Kaluza 2.1 (Beckman Coulter) or FlowJo v10.6 (BD Biosciences) software was used for data analysis.

Hematopoietic assays

$CD34^+$ HSPCs were thawed and expanded in StemSpan SFEM (STEMCELL Technologies) containing 1% penicillin/streptomycin (Gibco), 100 ng/mL SCF, 100 ng/mL FLT3L, 20 ng/mL IL6, 50 ng/mL TPO (cytokines from Peprotech), and 750 nM SR1 (STEMCELL Technologies) for 2 days prior to transduction. Cells were transduced in the presence of 4 μg/mL Polybrene (Sigma-Aldrich) on RetroNectin-coated plates (TaKaRa), using two consecutive rounds of super-concentrated virus. Four days post-transduction, the cells were sorted and plated in human methylcellulose complete medium HSC003 (R&D Systems) for colony-forming assays. Fifteen thousand cells were initially plated over two 6 mm dishes. The colonies were counted once they had reached a sufficient size (10–14 days).

For assays using patient-derived AML blasts, *in vivo* expanded samples were thawed and pre-cultured in StemSpan SFEM (STEMCELL Technologies) containing 1% penicillin/streptomycin (Gibco), 50 ng/mL SCF, 50 ng/mL FLT3L, 10 ng/mL IL6, 2.5 ng/mL IL3, 10 ng/mL TPO (cytokines from Peprotech), and 750 nM SR1 and 35 nM UM171 (both from STEMCELL Technologies) for 24–48 h. Transductions were conducted in the presence of 2 μg/mL Polybrene (Sigma-Aldrich). The cells were harvested 48 h post-transduction for xenotransplantation into mice or for colony-forming assays.

Animal experiments

Two-color *in vivo* competition experiments were performed in murine xenograft models of AML as previously described.[51,74] In brief, stable dCas9-KRAB cell lines or *in vivo* expanded patient-derived AML cells (PDXs) were transduced with E2Crimson or dTomato sgRNA vectors, mixed 1:1, and injected via tail vein into irradiated (2.5 Gy), 8–10 week old NOD.Cg-Prkdc^{scid} Il2rgtm^{1Wjl}/SzJ (NSG) recipients. One to two million cells were injected per mouse, and tracked via flow cytometry on peripheral blood samples every 4 weeks. The mice were sacrificed upon leukemia onset, at which point cells were isolated from the bone marrow, spleen, and liver, and analyzed by flow cytometry. An anti-human CD45 antibody was used to track AML cell lines, which were generated using the dCas9-KRAB.P2A.BSD construct (Addgene 90332). The PDXs were generated using the dCas9-KRAB.P2A.m.Neon construct (170482); thus, fluorescence-based tracking was sufficient. sgRNA-containing E2Crimson or dTomato cell populations were compared to determine relative proliferation. All mice were housed under a 12 h light/12 h dark cycle in a pathogen-free environment at the Martin Luther University Halle-Wittenberg. All animal procedures were approved by the local state authorities (Landesverwaltungsamt Sachsen-Anhalt).

RNA sequencing

RNA was isolated from cells using the Quick-RNA Miniprep Kit (Zymo Research) on days 3 and 6 or 7 post-transduction (for ML-2 and K562, respectively; the late time point was selected based on depletion kinetics in Figure 2C). PolyA-enriched total cellular RNA sequencing was performed by Novogene Company, Ltd. on an Illumina NovaSeq 6000 using 150 bp paired-end chemistry. The raw sequence data were processed by Novogene using a standard pipeline. In brief, reads were filtered using in-house scripts and mapped to human reference genome hg38 using HISAT2,[75] and gene expression was quantified using the featureCounts[76] function in R. Differential expression analysis was conducted in R using DESeq2[58] (Bioconductor). Gene sets from MSigDB v7.2 (H1, C2, C3, C6), custom hematopoietic[6] and chromosome 15 gene sets, and PAF1c-knockout expression signatures[28] were tested for enrichment using the Broad GSEA software.[61] Custom positional gene sets were generated by walking a 1 Mb or 5 Mb window along chromosome 15. Gene ontology analysis was carried out using the DAVID[77] functional annotation tool (https://david.ncifcrf.gov/summary.jsp).

Next generation Capture-C

Chromatin conformation capture with selective enrichment for *MYNRL15*-interacting sequences was performed using NG Capture-C as previously described,[22] with minor modifications: (1) 5–10 million cells were harvested per sample and DpnII digestion reactions were scaled down accordingly. (2) DNA was sheared to 200 bp using a Branson 450 Digital Sonifier (Marshall Scientific) (time 18 s, amplitude 20%, pulse 0.5 s, pause 1.5 s; repeat 5x). (3) All of the material from the first capture was used as input for the second capture. (4) The libraries were

sequenced by Novogene Company, Ltd. on an Illumina NovaSeq 6000 (150 bp paired-end reads). sgRNA-transduced K562 and ML-2 cells (day 3 post-transduction) and *in vitro* expanded CD34$^+$ HSPCs (day 3 post-thawing) were used to evaluate the effect of *MYNRL15* perturbation and the normal conformation of the locus, respectively. We used biotinylated oligonucleotides (sequences in Table S6) targeting a viewpoint in the candidate *cis*-regulatory region C1 to enrich for interactions involving the locus. Two biological replicates were prepared per sample and pooled prior to oligonucleotide capture.

The biotinylated capture oligonucleotides were designed using CapSequm2[64] (https://capsequm.molbiol.ox.ac.uk/cgi-bin/CapSequm.cgi) and purchased from Integrated DNA Technologies. Raw sequence data were processed with the capC-MAP package[65] using default settings. Normalized pileups (RPMs; binstep = 3000, window = 6000) were capped at the 99th percentile and scaled to the maximum signal within the sample, so that cross-sample comparisons could be made on a 0–1 scale. The data were visualized in the UCSC Genome Browser[67] using a smoothing window of 2 pixels, alongside CTCF ChIP-seq data from K562 cells (ENCODE accession no. ENCFF519CXF) and Knight-Ruiz matrix-balanced[78] Micro-C[79] data from H1-hESC cells. Hi-C data from Rao et al.[80] were also used to confirm the presence of specific 3D chromatin structures in other cell lines.

Dual luciferase assays

Dual luciferase assays were performed using the Dual-Luciferase Reporter Assay System (Promega). The candidate *cis*-regulatory regions C1 and C2 were cloned alone or in combination upstream of the minimal promoter in the pGL4.23 firefly luciferase reporter construct (Promega E8411). A pGL4.7 *Renilla* luciferase reporter construct (Promega E6881) driven from the EF1α promoter was used as a background control. The firefly and *Renilla* vectors were co-transfected into K562 cells at a 20:1 ratio via nucleoporation, using the Lonza 4D-Nucleofector and SF Cell Line X Kit S. 24 h post-transfection, cells were harvested and measured on a GloMax 96 Luminometer (Promega).

Quantitative real-time PCR

RNA was isolated from cells using the Quick-RNA Microprep or Miniprep Kits (Zymo Research), between days 3–5 post-transduction. RNA fractionation was performed as previously described,[81] except that we directly lysed the nuclear pellet instead of isolating the nuclear-soluble and chromatin-associated fractions separately. *B2M* and *XIST* were utilized as cytoplasmic and nuclear controls, respectively. The TURBO DNA-free Kit (Invitrogen) was used for DNase treatment. Total cDNA was synthesized using the High-Capacity cDNA Reverse Transcription Kit, and gene expression was quantified by real-time PCR using SYBR Select Master Mix and gene-specific primers on a StepOnePlus Real-Time PCR cycler (all products from Applied Biosystems). *B2M* was used as a housekeeping control. Primers for qRT-PCR can be found in Table S6. QuantiTect primer assays were used to detect *WDR61* and *IMP3* (Qiagen QT00083776 and QT00232330).

CRISPR-Cas9 indel and excision validation

PCR-based methods were used to validate CRISPR-Cas9 mediated insertions and deletions (indels; to knock out protein-coding genes) and *MYNRL15* excision via paired sgRNAs. Cells were harvested between days 3 and 5 post-transduction, and genomic DNA was isolated using the Quick-DNA Miniprep Kit (Zymo Research). We relied on TIDE[56] (tracking of indels by decomposition) to assess knockout efficiency; thus, we PCR amplified ~700 bp genomic regions centered on the corresponding sgRNA target sites from knockout and control (wild type) samples. The resulting products were subjected to Sanger sequencing, and knockout and wild type sequences were compared in the TIDE[56] online tool (http://shinyapps.datacurators.nl/tide/). To validate *MYNRL15* excision, we performed PCR using primers flanking the region to be excised, thereby allowing us to ascertain deletion based on the size of the PCR product. All PCR primer sequences can be found in Table S6.

TCGA/TARGET

RNA-seq data from adult and pediatric AML patient cohorts were obtained from TCGA[82] (https://gdc.cancer.gov/access-data) and TARGET[83] (https://ocg.cancer.gov/programs/target/data-matrix), respectively. DESeq2 (Bioconductor) was used to normalize and variance-stabilize read count data.[58] The TARGET dataset also required batch correction, for which we used sva[59] (Bioconductor). Normalized (and batch corrected) expression values were used for subsequent analyses. Unsupervised clustering was performed using Rtsne[60] (base R).

QUANTIFICATIONS AND STATISTICAL ANALYSIS

Statistical evaluations of experimental data were carried out in GraphPad Prism 9 using two-tailed, unpaired t tests. Data are presented as mean $\pm$ SD or SEM. as indicated in the figure legends. Statistical analyses of gene expression data (RNA-seq) were carried out in R using DESeq2,[58] or via the Broad GSEA software.[61] CRISPR-Cas9 screening data were analyzed using MAGeCK[18] to call essential genes, with the exception of the tiling screens, which were analyzed in R using DESeq2. Differences with $p < 0.05$ were considered significant. Sample sizes are indicated in the figure legends. No statistical methods were used to predetermine sample size.